AN ABSTRACT OF THE DISSERTATION OF

Patrick Warren Monigle for the degree of Doctor of Philosophy in Geophysics presented on September 12, 2014.

Title: Seismic Wave Attenuation of the Crust and Upper Mantle in the Himalaya and South-Central Tibetan Plateau

Abstract approved:

John L. Nabelek

Recent geophysical and geological investigations of the Tibetan plateau have given rise to conflicting models of plateau growth and deformation, where the presence and extent of partial melt in the crust could be a determining factor. Here we investigate the attenuation structure of the crust and upper mantle, as attenuation is particularly sensitive to temperature and fluids, both aqueous and melts. We present 3D Q_p and Q_s results of attenuation structure beneath the HiCLIMB array using local earthquakes recorded between 2004 July and 2005 August. Additional synthetic data analysis shows our ability to expand attenuation analysis beyond the traditional use of first-arriving seismic phases to include reflected and refracted arrivals from the Moho and a persistent upper crust velocity interface. Synthetic analysis also reveals a bandwidth-limited window over which source and attenuation can be uniquely

determined, improving the precision of attenuation measurements. Results indicate a high $Q_{p,s}$ upper crust, interrupted by moderate to low Q_p faulting and evidence for partial fluid saturation to depths of 15 km and full saturation before 30 km depth. Middle and lower crust attenuation is broadly low $Q_{p,s}$, with evidence for limited partial melt and interrupted by high $Q_{p,s}$ bodies near the termination of the subducting Indian plate and coincident with a sharp decrease in upper mantle Q_p. We find little evidence for extensive partial melt in the crust and the sharpness of Q transitions at depth coincident with changes in faulting style in the upper crust suggest strike-slip motion penetrates the crust and upper mantle at the terminus of subduction.

Seismic Wave Attenuation of the Crust and Upper Mantle in the Himalaya and South-Central Tibetan Plateau

by

Patrick Warren Monigle

A DISSERTATION

submitted to

Oregon State University

in partial fulfillment of
the requirements for the
degree of

Doctor of Philosophy

Presented September 12, 2014
Commencement June 2015

Doctor of Philosophy dissertation of Patrick Warren Monigle presented on September 12, 2014

APPROVED**:**

Major Professor, representing Geophysics

Dean of the College of Earth, Ocean and Atmospheric Sciences

Dean of the Graduate School

I understand that my dissertation will become part of the permanent collection of Oregon State University libraries. My signature below authorizes release of my dissertation to any reader upon request.

Patrick Warren Monigle, Author

ACKNOWLEDGMENTS

First and foremost, I would like to thank John Nabelek and Jochen Braunmiller for their support and guidance over the past few years. Their knowledge and passion is limitless and they have been fantastic role models for the type of scientist I hope to be in the future. Gary Egbert, Andrew Meigs, and David Finch have served as outstanding committee members, being willing to meet on short notice and provide critical and constructive feedback whenever necessary. In addition to the above, Anne Trehu, Rob Harris, and Adam Schultz have contributed greatly to my development while at OSU. I also want to thank Del Bohnenstiehl, my advisor at NC State, as his passion and support has set me on this career path, and he continues to be a close mentor.

My time in Oregon would not have been as successful and enjoyable without many members of the Corvallis community and my fellow graduate students. In particular, Evan and Mark were outstanding to work alongside and were just as enjoyable outside. My soccer and running friends will never be forgotten (nor their pets), and especially those who crossover. I also want to thank Erik and Erin, as no matter how much time passes between visits, we are always able to pick up right where we left off, and I look forward to more celebrations in the future.

Most importantly, I wish to thank my family. My parents' and my brother's unwavering support over the years has been instrumental to my success as a student and my development as a person. They have provided me confidence when I have wavered, they have asked, "When do you plan to finish" when I have been distracted, and they have encouraged me to follow my passion since the very beginning. The rest of this would not be possible without them and I will be forever grateful.

CONTRIBUTION OF AUTHORS

Dr. Jochen Braunmiller contributed intellectually to the experimental design, interpretation of data, and editing processes for all chapters and appendices. N. Seth Carpenter contributed the starting phase catalog for Appendix 2.

TABLE OF CONTENTS

Page

LIST OF FIGURES

LIST OF FIGURES (Continued)

Figure Page

LIST OF TABLES

LIST OF APPENDICIES

Seismic wave attenuation of the crust and upper mantle in the Himalaya and South-Central Tibetan Plateau

Patrick W. Monigle[1], John L. Nabelek[1], Jochen Braunmiller[1,2]*

[1]Oregon State University, College of Earth, Ocean, and Atmospheric Sciences, Corvallis, Oregon, USA

[2]Now with University of South Florida, College of Arts and Sciences, Tampa, Florida, USA

*Corresponding author e-mail: pmonigle@coas.oregonstate.edu

In preparation for submission to Journal of Geophysical Research

American Geophysical Union

2000 Florida Ave. NW, Washington, DC, USA

1. SEISMIC WAVE ATTENUATION OF THE CRUST AND UPPER MANTLE IN THE HIMALAYA AND SOUTH-CENTRAL TIBETAN PLATEAU

1.1 Scientific Motivation

The HiCLIMB seismic array operated between 2002-2005 and occupied 230 sites along a dense north-south linear array, and a smaller, sub-network of stations of southern Tibet and Nepal [Nabelek et al., 2009]. The overarching goal of the experiment was to examine the lithosphere-scale dynamics of the ongoing India-Eurasia collision that has produced the Himalaya and Tibetan plateau. Major results of the HiCLIMB experiment to date include a receiver function model imaging the Indian lithosphere underthrusting Tibet for more than 400km [Nabelek et al., 2009] and several local and regional earthquake catalogs with high quality locations, and in some cases, moment tensor analysis of the seismic sources [e.g. Baur, 2007; Carpenter, 2010; Nabelek et al., 2011; Monigle et al., 2012]. The goals of this dissertation are: 1) investigate, improve, and expand the methodology of calculating attenuation through the use of synthetic data, ensuring the highest quality data is used for the geophysical inversion; and 2) utilize the dense array of earthquakes and seismic stations to image fine scale attenuation structure, contributing a unique perspective to our lithosphere scale imaging and improve our understanding of the dynamics of the collision. The remainder of the Motivation will focus on background information

pertinent to experimental and analytical decisions that may not be explained fully in the body of the dissertation, which was kept concise for the purpose of future publication. This dissertation additionally includes a previously published manuscript (Monigle et al., 2012) in Appendix 2, which closely examines a region of persistent earthquake activity in southern Tibet, providing high-precision earthquake locations, moment tensor analysis, and an interpretation of the earthquake sequence as it pertains to global patterns of normal faulting. The data from this earlier study is included in the attenuation analysis and was used to test parts of the methodology.

Attenuation analysis was chosen for two reasons: 1) attenuation provides unique information related to the physical state of the crust and upper mantle that is not included in traditional seismic velocity tomography investigations, and 2) the international explosion monitoring community is interested in the attenuation of seismic phases in regions of poor crustal propagation. This dataset provides a dense array of seismic stations and extensive local, well-located earthquakes that allow for the determination of fine scale attenuation structure across the Himalaya and Tibetan plateau, a level of resolution not typically available in high-interest regions [Nabelek et al., 2011]. The fine-scale analysis and improvements in methodology can allow the monitoring community to improve seismic discrimination and yield estimates in other high attenuation regions of interest [e.g. Hartse et al., 1997]. From a tectonic perspective, the attenuation structure provides important information about the competency of the geological material and the presence and extent of fluids, including

both partial melt and aqueous fluids, which have strong implications for deformation mechanisms within the plateau.

On a general scale, attenuation is a measure of the energy loss per cycle of elastic wave motion. Seismic waves must decrease in amplitude as they propagate to account for an expanding energy front. This phenomenon is known as geometrical spreading and does not result in energy loss and is thus considered an elastic process. Scattering and multipathing are also elastic processes that result from seismic waves traversing heterogeneous media and shift the arrival of seismic energy, usually into the coda of the seismic phase. The goal of most attenuation studies is to measure the anelastic process, intrinsic attenuation, in which energy is converted to heat and lost through permanent deformation on a macroscopic scale. On a microscopic scale, grain boundary sliding and the flow of fluids across grain boundaries are important sources of energy loss [Stein and Wysession, 2003]. While measuring the amplitude of seismic waves is straightforward, attenuation is a frequency dependent measurement calculated from spectra and separating the effects of the seismic source, elastic, and anelastic effects along the ray path is very difficult.

There are two main approaches to measuring the attenuation of seismic waves over local to regional distances: 1) coda wave measurements and 2) body wave measurements. Coda wave measurements are typically associated with the L_g or P_g phases [e.g. Xie 2002; Xie et al., 2004; Bao et al., 2011] at regional propagation distances ($\gtrsim$300 km). Spectra of the arriving wave and its coda are measured and the observed attenuation represents that of the wave-guide (upper crust for L_g, P_g, mantle

lid for P_n, S_n) through which the phase has traveled, providing a 1D measure of attenuation along the ray path. This method almost exclusively involves a ratio of spectra from a single event recorded at two stations, thereby eliminating source effects, a large source of error otherwise, and measuring attenuation in the region between those stations. By utilizing ratios involving multiple stations and events (a range of which are well described in Ford et al., 2008), resolution can approach 1° in a 2D sense (map view) [e.g. Bao et al., 2011], but coda studies are unable to access attenuation as a function of depth. Higher resolution and 3D analysis, however, can be obtained by narrowing the time window over which the spectra is calculated, focusing only on the discrete body wave arrival, allowing for accurate mapping of the ray path with depth [e.g. Eberhart-Phillips et al., 2005; Hauksson and Shearer, 2006; Sheehan et al., 2013]. This method requires a correction for the frequency-dependent seismic source, which can impart large error on the data specifically for small earthquakes, where the source cannot be isolated from attenuation effects, and for large events, which can have complex rupture patterns. The HiCLIMB array is ideally suited for coda studies because its linear arrangement is optimally oriented for inter-station ratios. However, the lateral array, close station spacing, and dense earthquake distribution provide excellent resolution capabilities for the body wave method and best take advantage of the unique dataset. The Methods of this dissertation research are particularly sensitive to reducing and/or eliminating the source-attenuation tradeoff to improve the overall quality of analysis.

Tibet provides a unique setting for attenuation studies because of its importance to the monitoring community and because it provides information about the physical state of the crust and mantle in one of the most severely attenuating continental regions in the world [Xie 2002; Xie et al., 2004]. In typical continental regions, attenuation values range from Q~200 in tectonically active regions, where rock is highly fractured and fluids are abundant, to 650 or higher in stable regions with competent rock [e.g. Mitchell, 1995]. This range of values have a clear observable manifestation: a magnitude 6 earthquake in California is only felt state-wide (Q~200) whereas the earthquake in Mineral, Virginia (Q>650) is felt throughout the eastern United States as documented in USGS earthquake felt reports (earthquake.usgs.gov). In Tibet, this range of values is observed over limited geographical distances and represents a combination of the geological composition, fluid content, and the thermal state of the region.

1.2 Abstract

Recent geophysical and geological investigations of the Tibetan plateau have given rise to conflicting models of plateau growth and deformation, where the presence and extent of partial melt in the crust could be a determining factor. Here we investigate the attenuation structure of the crust and upper mantle, as attenuation is particularly sensitive to temperature and fluids, both aqueous and melts. We present 3D Q_p and Q_s results of attenuation structure beneath the HiCLIMB array using local

earthquakes recorded between 2004 July and 2005 August. Additional synthetic data analysis shows our ability to expand attenuation analysis beyond the traditional use of first-arriving seismic phases to include reflected and refracted arrivals from the Moho and a persistent upper crust velocity interface. Synthetic analysis also reveals a bandwidth-limited window over which source and attenuation can be uniquely determined, improving the precision of attenuation measurements. Results indicate a high $Q_{p,s}$ upper crust, interrupted by moderate to low Q_p faulting and evidence for partial aqueous fluid saturation to depths of 15 km and full aqueous saturation before 30 km depth. Middle and lower crust attenuation is broadly low $Q_{p,s}$, with evidence for limited partial melt in the lower crust and interrupted by high $Q_{p,s}$ bodies near the termination of the subducting Indian plate and coincident with a sharp decrease in upper mantle Q_p. We find little evidence for extensive partial melt in the crust and the sharpness of Q transitions at depth coincident with changes in faulting style in the upper crust suggest strike-slip motion penetrates the crust and upper mantle at the terminus of subduction.

1.3 Introduction

The Himalaya and Tibetan plateau represents one of the largest physiographic features in the world, the development of which likely had global implications for tectonic plate motion [Copley et al., 2010] and climate [Ruddiman and Kutzbach, 1989]. The geological history of the India-Eurasia plate boundary is well constrained

and described in literature. The Tibetan plateau, with an average elevation of 5 km, is composed of accreted microcontinents and island arcs that record the southward march of the convergent zone since subduction along the Eurasia margin began in the early Paleozoic [Yin and Harrison, 2000]. Currently, the front of the convergent boundary is the Main Frontal thrust (MFT, Figure 1), with the Indian plate descending below the Himalaya along the gently dipping Main Himalaya thrust (MHT). The MHT can be traced more than 400 km north of the MFT [Nabelek et al., 2009], crossing more steeply beneath the Yarlung-Tsangpo suture (YTS), which represents the surface relic of the Neo-Tethys Sea and the Indo-Eurasia convergence zone around 65 Ma, and terminating within the Lhasa terrane, an ancient microcontinent once rifted from Gondwana [Zhu et al., 2011]. Seismic imaging detects a flat Moho more than 70 km deep in the Lhasa terrane, which shallows in a step-like fashion to 65 km depth farther north near the Bangong-Nujiang suture (BNS) and remains constant under the Qiangtang block [Kind et al., 2002; Nabelek et al., 2009]. Each of the geological terranes record a intricate history of rifting, deposition, uplift, and intrusion related to a complex subduction and accretion history [Yin and Harrison, 2000], which have been further deformed by the continued convergence of India and Eurasia since ~40 Ma [Molnar and Tapponnier, 1975].

Earthquakes and geophysical imaging techniques provide an instantaneous view of the long-standing processes involved in mountain building, plateau development, and expansion, yielding evidence of how the region is currently deforming [i.e. Molnar, 1984]. Shallow earthquake activity indicates dominantly

convergent deformation along the MFT and Himalaya arc, with pervasive extensional faulting in southern Tibet and a transition to strike-slip motion in northern Tibet. Deep earthquakes track the subducting India plate and indicate upper mantle deformation in the region. In southern Tibet, the INDEPTH experiments were the first to document seismic low velocity zones (LVZ) and "bright spots" in the crust under the Yadong-Gulu rift, which were interpreted as evidence for a partially molten middle crust [Nelson et al., 1996; Kind et al., 1996; Makovsky and Klemperer, 1999]. Coincident with these seismic experiments, magnetotelluric (MT) data imaged zones of high conductivity, indicating partial melt and/or aqueous fluids were likely pervasive in the crust at depths below 20-30 km [Wei et al., 2001; Unsworth et al., 2005]. As a corollary to these observations, thermal-mechanical models of channelized flow were developed to explain the outward growth of the plateau- invoking a low viscosity channel from a partially molten middle and lower crust allowing material to escape outward [Beaumont et al., 2001; Beaumont et al., 2004; Klemperer, 2006]. However, the spatial pattern of thrust, normal, and strike-slip faulting at the surface is consistent with mechanical models whereby the upper crust is mechanically coupled to the obliquely subducting Indian lithosphere below, implying a strong lower crust [McCaffrey and Nabelek, 1998; Copley et al., 2011]. In this model, the traction force of oblique motion at depth is coupled to the upper crust, which would preclude a low viscosity channel and extensive partial melt within the crust.

One way to search for evidence of extensive partial melt in the Tibetan crust is to measure the attenuation, or decay, of seismic waves as they propagate through the

Himalaya and Tibetan plateau. Attenuation is a measure of the amount of energy lost per cycle of an elastic wave ($\Delta E = -2\pi E/Q$) and described as the quality factor (Q), so that regions of efficient seismic propagation are high Q (low $1/Q$) and areas described as low Q (high $1/Q$) are highly attenuating. In dry rock, attenuation is driven by grain boundary sliding and is highly dependent on temperature, pressure, and composition [Jackson, 2000; Jackson et al., 2002]. In wet rock, containing aqueous fluids or melt, fluid flow along pores and grain boundaries are important and depend on fractures, porosity, and permeability [Toksoz et al., 1979; Winkler and Nur, 1979; Mavko, 1980; McCarthy and Takei, 2011]. In regional settings attenuation can vary over orders of magnitude. In New Zealand and the Andes, Q values as low as the 10s have been identified under magmatic arcs associated with melt and fluid pathways, while Q values approaching 1000 are associated with the subducting slab and underlying mantle [Haberland and Rietbrock, 2001; Schurr et al., 2003; Eberhart-Phillips et al., 2005]. A similar range of Q values (50-1200) is observed within the upper crust in southern California representing the attenuation behavior of deep sedimentary basins (low Q) to batholithic terranes (high Q) [Hauksson and Shearer, 2006]. Previous attenuation studies within the southern Tibetan plateau have examined the 1D propagation efficiency of seismic phases L_g and P_n, documenting severe S-wave (L_g) attenuation ($Q \leq 100$) in the upper crust and a range of P-wave values (Q=180-375) in the upper mantle [Xie, 2002; Xie et al., 2004; Xie 2007]. A region of inefficient S_n propagation in central Tibet north of the BNS has also been observed [Barazangi and Ni, 1982]. Recently, Sheehan et al., [2013] examined the attenuation structure under

the Himalaya and observed high attenuation in the middle and lower crust with evidence for high fluid concentrations in localized areas.

In this study, we present path integrated (t^*) attenuation tomography, which best takes advantage of our dense distribution of stations and earthquakes (Figure 1) to provide high-resolution attenuation structure with depth. We expand the traditional use of t^* to include reflected and refracted phases in order to provide additional ray coverage in the middle and lower crust to help identify the presence or absence of melt, clarifying the potential existence of a low viscosity channel. We present a thorough analysis of synthetic data, documenting a required differentiation of refracted-wave data and a restricted bandwidth over which the seismic source can be uniquely isolated from the effect of attenuation. Our results provide evidence for the partial and full saturation of aqueous fluids in the upper crust and increased attenuation associated with well-developed normal and transform faults. We do not find evidence of extensive melt within the middle and lower-crust, though there may be evidence for a thin layer of partial melt in the lower crust. A sharp transition from low to high attenuation in the upper mantle is observed at the termination of the subducting Indian plate (SIP), with sharp attenuation transitions similarly observed in the lower and upper crust. These results may indicate strike-slip motion on a lithospheric scale, dividing the Tibetan crust and SIP material to the south from Eurasian material to the north. As a whole, results suggest mechanical coupling [McCaffrey and Nabelek, 1998; Copley et al., 2011] plays an important role in plateau deformation.

1.4 Data and Methods

1.4.1 HiCLIMB Data

Attenuation analysis focused on Phase-2 (2004 July to 2005 August) of the HiCLIMB experiment [Nabelek et al., 2009], which consisted of 75 stations at 8 km intervals along an approximately linear 600 km array stretching south of the YTS to north of the BNS. A 38-station network flanked the linear array to the east and straddled the YTS with 30-40 km station spacing (Figure 1). Seismometers of the main array recorded at 50 samples-per-second (sps), while the lateral array operated at 40, 50, or 100 sps. Local and regional earthquake locations and associated seismic phases were selected from the catalogues of automatic picks [Carpenter, 2009; Riddle et al., 2014a, Implementation of an Automatic Polarization *S* wave Picker for Local Earthquake Tomography in South-Central Tibet, manuscript in preparation], as well as the manually picked, high-precision catalogues of Nabelek et al., [2011] and Monigle et al., [2012].

Earthquakes for this study were initially selected based on M_L>2.5 and having more than 50 associated phases (Figure 1, white dots). The catalog was reduced based on data quality and other factors discussed later under Methods. The final catalog is supplemental Table S1. Events span M_L 2.4-5.1, ranging in location from the surface to 90 km depth, with events clustering in the upper crust (<20 km depth) and below the Moho. Deep events below the Moho to 90 km depth (blue in Figure 1) are limited

to the south and southeast, while shallow events (red and green) are located throughout the study area. In total, more than 2,600 phases were analyzed from 46 events and almost 1,600 phases were included in the inversion.

*1.4.2 Spectra and t**

Vertical (*P*) and transverse (*S*) seismograms (measuring ground velocity) were high-pass filtered at 0.2 Hz, reducing low-frequency noise and avoiding the measurement band, and data from a 3.4 second time window centered on the arrival time were treated with a hanning window and extracted (Figure 2). This time window was selected to include the full source duration while limiting the influence of energy not associated with the predicted ray path. The hanning window further isolates the energy from the arriving phase. If the earthquake source was not fully captured, the window was expanded to 5 seconds length, remaining centered on the arrival. A background noise level was established over an identical length (3.4 or 5s) time window for consistency, immediately preceding the primary *P* window. Time series data were transformed to spectra, corrected for instrument response, and fit between 0.5 Hz and the band limit based on the sample rate of the instrument (18 Hz, 20 Hz, or 40 Hz). Spectra were smoothed over a moving 1 Hz bin prior to evaluating for source and attenuation. All treatment of time series and spectral data were tested using synthetic data to ensure they do not affect the attenuation measurement.

Attenuation is evaluated through the *t** attenuation operator, which is a measure of the path integrated attenuation. The absolutely ground velocity spectrum

(A_{ij}) from the i^{th} event recorded at the j^{th} station is described in Equation 1 [after Schurr et al., 2003; Eberhart-Phillips et al., 2005]. The absolute spectrum measured at a station has contributions from a frequency-independent geometrical spreading and source seismic moment contained in Ω_0, a frequency dependent source spectrum (S_i), and attenuation (t^*) along the ray path.

$$A_{ij}(f) = 2\pi f \Omega_0 S_i(f) exp\left[-\pi f t_{ij}^*\right] \quad (1)$$

The attenuation operator, t^*, is defined as a an integral of the inverse of the product of medium velocity $V(r)$ and quality factor $Q(r)$ over the distance traveled along the ray path (dr).

$$t^* = \int_j^i \frac{dr}{V(r)Q(r)} \quad (2)$$

The attenuation calculated includes both intrinsic and scattering attenuation and should be considered a total Q. As is common in t^* studies [e.g. Abercrombie, 1995; Hauksson and Shearer, 2006], attenuation is treated as frequency independent, which is appropriate in this study given the narrow frequency band of the measurements and the goals of this investigation. A Brune [1970] source spectrum (Equation 3: B_i) is assumed for t^* calculations, with f^2 decay beyond a corner frequency (f_c) that scales with the moment of the seismic source [Abercrombie, 1995; Shearer et al., 2006].

$$S_i(f) = B_i = \frac{1}{1 + (f/f_{ci})^2} \quad (3)$$

The source spectrum and attenuation are calculated from the observed spectrum by substituting Equations 2 and 3 into Equation 1 and rearranging to form Equation 4. The resulting equation describes the recorded spectra as a product of three parameters: 1) an event specific source (f_c), 2) a station specific spectral level (Ω_0), and 3) path dependent attenuation (t^*). We later invert t^* values from each ray path for the underlying attenuation structure (Q^{-1}) with knowledge of the velocity structure.

$$\ln\left(A_{ij}(f)\right) - \ln(2\pi f) - \ln\left(\frac{1}{1 + (f/f_{ci})^2}\right) = \ln\left(\Omega_0\right) - \pi f t_{ij}^* \quad (4)$$

1.4.3 Source and attenuation tradeoff

In any t^* estimate, there is an inherent tradeoff between the spectral falloff that results from an earthquake source and decay through attenuation. For decreasing earthquake magnitude, an increase in source f_c is expected [e.g. Abercrombie, 1995; Shearer et al., 2006], which effectively shifts the source-related spectral falloff to higher frequencies (Equation 3; Figure 3, inset). As a result, for earthquakes considered small for this study ($M \lesssim 3$), the expected source corner can approach the available band limit (~20 Hz). Depending on the available spectral bandwidth, it can be impossible to determine a unique source and attenuation model, as an increase in f_c

can be offset by an increase in attenuation that would result in nearly identical spectra (Figure 3). This tradeoff is not adequately discussed in current literature and we utilize synthetic spectra to investigate the frequency range over which we can accurately separate the effects of source and attenuation, preventing the inclusion of non-unique data in the inversion.

A synthetic example demonstrates the expected spectra for a range of Brune sources (Equation 3) at 100 km distance, traversing a medium with a uniform velocity and attenuation structure (Q=450), and recorded at a station with a sample rate of 40 sps (Figure 3A, inset). A sample rate of 40 sps is utilized because it provides a 19.5 Hz bandwidth (0.5-20 Hz) for fitting, which is standard for most data in this study, consistent with a 50 sps instrument after accounting for digital decimation. Data are shown with source corner frequencies stepping between 5-50% of the Nyquist frequency (1.25-10 Hz for inset example). Synthetic spectra are inverted for a best-fit source corner frequency (f_c) over the range 0.1-20 Hz using a standard grid search method [e.g. Schurr et al., 2003; Eberhart-Phillips et al., 2005], which is the same approach we use with observed data. Misfit is calculated for each f_c and the residuals are plotted in Figure 3A. The residual values are plotted as a function of Nyquist normalized f_c because the relationships hold across all instrument sample rates (or available data bandwidth). The f_c-Q pairs shown are results for the inset spectra (f_c=10 Hz, 50% Nyquist), where a range of source/attenuation pairs result in spectra with no discernable difference in residual. The choice of distance and attenuation model is not important for corner frequency resolution, as this is dependent only on the available

bandwidth (Figure 3A). For events where the corner frequency is not resolved, however, the amount of error in modeled attenuation does change as a function of distance and Q structure (Figure 3B). The Q percent error in Figure 3B represents the difference in the input model Q with the inversion result for a 20 Hz source, which is a common source result for smaller magnitude events when the source is not resolved, or, if the instrument response is not properly treated, as there is a strong spectral roll-off near 20 Hz for 40 and 50 sps instruments. Figure 3B shows inverted Q values within 10% of the input model as solid lines, within 20% as short-dash lines, and beyond 20% as long-dash lines. For instruments near the source of a small event, an incorrect source can result in Q values that are half the true value in high Q environments. This effect is decreased at longer distances and in higher attenuating regions. Additionally, as bandwidth increases beyond 19.5 Hz, the error curves are reduced.

For analysis of observed seismic data, we apply a rigorous procedure to determine a single, best-fit source (f_c) for each event analyzed (Table S2) over the corner frequency range 0.1-20 Hz. We include all arrivals with at least a 15 Hz bandwidth above twice the noise level and additionally require a minimum of 3 stations to establish an event f_c to ensure a well-resolved source. The best-fit f_c is the minimum of the summed residuals for qualifying spectra across all stations for a single event. Individual spectra are not considered if the best-fit f_c is 0.1 Hz or above 15 Hz, as this can be consistent with poor data quality or other factors. Stations with significant low-frequency contamination can result in a best-fit f_c of 0.1 Hz, which

would imply a seismic source approaching M≳5 and not appropriate for smaller magnitude events. For stations with a best-fit f_c above 15 Hz, this is typically consistent with the radiation pattern of the source, as nodal stations can exhibit a "flat" spectrum, spurious narrow-band enrichment from local environs, or a source in which the corner frequency cannot be accurately constrained. The 15 Hz cutoff is reduced or expanded based on earthquake magnitude and the availability of 100 sps data, which can accurately determine f_c>10 Hz. Once determined, the best-fit source was visually evaluated for fit at near-epicentral stations, where the effects of attenuation are reduced. If the source is unresolved or poorly resolved, the event was not used and our starting catalogue was reduced. Figure 4 displays the relationship between magnitude and corner frequency for this dataset. Note there are no corner frequency greater than 10 Hz and our minimum magnitude for direct use is M_L 2.5. We do not calculate a unique corner for *S* phases in this study due to limited *S* observations and instead use f_c^P. Whereas the Brune model represents small, simple earthquake sources well, natural earthquakes contain complexities that are not modeled. To prevent the further propagation of error, we do not scale f_c^P to match observed f_c^P - f_c^S relations, as the exact relationship has not definitively been determined [Abercrombie 1995; Shearer et al., 2006].

1.4.4 Attenuation calculation: t and SPMS*

Having established an accurate source f_c, the t^* attenuation parameter is now calculated for all available spectrum (per event) using Equation 4. In Equation 4,

recorded spectrum are integrated to displacement and then corrected for the best-fit Brune source spectrum (left side of Eq. 4). The resulting signal is then fit with a least squares line where the slope is proportional to t^* and includes a scalar spectral level (Ω_0). Figure 2 shows an example of data that has been fit using this procedure. Signal is only considered between 0.5 Hz and the instrument-dependent band-limit as described previously. Spectra must be above twice the pre-*P* noise level to be fit, or the bandwidth is reduced accordingly. Analysis is only performed if the signal bandwidth exceeds 3.0 Hz. Each spectra were visually evaluated for poor t^* values, generally related to anomalous spectral peaks or values close to zero. Anomalous spectral peaks were the result of local noise sources (high or low frequency) and would result in anomalous *Q* values for isolated stations. Values close to zero, implying $Q>1500$, were limited to near epicentral stations, where the effect of attenuation was reduced, and data with limited bandwidth, typically at long distances and/or for refracted arrivals. The mean signal bandwidth of the dataset for both *P* and *S* waves is approximately 14 Hz.

To improve the overall quality of the t^* measurements, a spectral ratio technique is utilized whenever possible to reduce error associated with complexities of the seismic source. In southern Tibet, there are several fault systems that exhibit persistent earthquake activity [e.g. Monigle et al., 2012]. For 13 of these event clusters (Figure 1, red circles), a single path, multiple-source ratio technique (SPMS) is used [after Fisk and Phillips, 2013]. SPMS assumes that the ray paths for two nearby events recorded at the same receiver will be identical. In taking a ratio of the spectra from the

two events, all path dependent and site dependent terms will cancel, resulting solely in a ratio of the two frequency-dependent event sources:

$$\Delta S_{1R}(f) = \frac{A_1(f)}{A_R(f)} = \frac{S_1(f)exp[-\pi f t^*]}{S_R(f)exp[-\pi f t^*]} = \frac{S_1(f)}{S_R(f)} \quad (5)$$

The ratio (ΔS_{1R}) is a function of frequency, with A_1 and A_R displacement spectra from two nearby earthquakes recorded at a single station. Reference event (A_R) has known (well-fit) Brune source (Eq 3: S_R=B_R). In Equation 5, we do not consider the source spectral level (Ω_0), as it is frequency independent. The spectra, A_1, can then be redefined combining Equations 1 and 5 and used to determine t*:

$$A_1 = B_R \Delta S_{1R} \Omega_0 exp\left[-\pi f t_{ij}^*\right] \quad (6)$$

As a result, using Equation 6 the complexity of the source is removed, including the radiation pattern, leaving solely the path integrated attenuation. The median inter-event epicentral distance for the SPMS event catalog is 1.4 km and SPMS t* values account for 50% of *P*-phase data. SPMS was not utilized for *S*-wave spectra due to limited observations.

1.4.5 Additional seismic phases

Seismic data for t^* calculations previously have relied on first-arriving phases for *P* and *S* waves and are generally restricted to direct P_g or S_g waves. In at least one study, refracted arrivals are incorrectly treated as direct phases [Sheehan et al., 2013]. In southern Tibet, earthquakes exhibit prominent, discrete arrivals associated with reflections and refractions from a persistent interface in the upper crust and the Moho (Figures 5,6). These reflections have been observed in northeast Tibet as well [Zhao et al., 2001]. This study seeks to expand the methodological approach of t^* attenuation modeling in order to improve resolution by incorporating these additional seismic phases. Synthetic data are used to demonstrate the ability to use reflected and refracted seismic phases to provide additional attenuation data at depth.

The Monigle et al. [2012] study provided a travel-time based velocity model from manual *P* and *S* phase picks (first-arrivals) traversing this study region (Figure 5). Synthetic seismograms [Bouchon, 1982] were generated based on this velocity model and a user-defined attenuation structure to determine the capability of isolating distinct seismic phases and identify their sensitivity to the attenuation structure (Figure 6). A synthetic example is provided for a source at 10 km depth. Velocity time series data are generated for a Brune 4.5 Hz source and include uniform attenuation (Q=450). Synthetic data are treated as described throughout the methods (i.e. windowing, smoothing, etc.).

The synthetic data exhibit a direct, up-going phase (P_g) to a distance of 230 km as the first arrival (Figure 6). Beyond 230 km, the first arriving phase becomes a down-going, refracted arrival. For a limited distance between 230 and 310 km, this

phase is refracted along the 28 km depth velocity interface (P_2) and beyond 310 km, the first arrival is a mantle-refracted wave (P_n). Synthetic and observed seismic data additionally exhibit two strong, persistent reflected phases. A reflection from the 28km interface (P_iP) is clearly prominent between approximately 100-200 km epicentral distances and a mantle reflection (P_mP) is distinct over a wide range of distances.

The synthetic data additionally show the changing character of the arriving phases. In Figure 6, direct arrivals exhibit a clear doublet waveform and reflected phases exhibit a similar shape, though the reflected arrival exhibits a phase shift that increases with increasing incidence angle. Refracted phases, however, are integrated [Aki and Richards, 1980] and appear as a discrete pulse. As a result, to accurately assess attenuation for any refracted phases, Equation 1 must be differentiated or the attenuation measurement will be overestimated (lower Q). In Figure 6F, the integrated spectra, as would be recorded, are shown in black and represent a 25% decrease in measured Q using a 4.5 Hz source (red dash line). As refracted phases travel along the velocity interface, we additionally test the depth to which the wave interacts with the attenuation structure of the underlying material, which we will refer to as the skin depth. These results are shown in Figure 7. We test the skin depth by modeling a non-attenuating crust (Q_c=10,000) and high attenuation mantle half space (Q_h=100), with a non-attenuating (Q_s=Q_c) buffer layer (mantle velocity) at the top of the upper mantle and invert solely for the attenuation of the refracted mantle leg (Q_m). By varying the thickness (Δ) of the buffer layer and inverting, synthetic data indicates phases refracting along a constant velocity layer are attenuated by the material in the higher

velocity layer and sample at most 3-5 km depth below the interface, depending on the magnitude of the velocity discontinuity. In all cases, the spectral decay is the summed effect of the distance traveled through the mechanical properties of each layer (velocity, Q), as described in Equation 2.

Whereas the majority of the data resides in the uppermost crust from direct, up-going phases, the inclusion of down-going phases improves the data coverage in the middle and lower crust dramatically. Including reflections from the 28km interface and the Moho represents only 20% of the phase count in the catalog, but provides 50% of the travel time in the middle crust (15-33 km) and 40% of travel time in the lower crust (33 km-Moho). Reflected and refracted phases account for 70% of the travel time below 15 km depth and allow for improved data coverage in the lower crust and upper mantle, which would otherwise only be sampled by deep events, or inaccurately accessed in the case of un-differentiated refracted phases.

1.4.6 Inversion

In order to assess the 3D attenuation structure, the region is divided vertically and laterally into cells. Vertical grid cell spacing was chosen so that a combination of direct, reflected, and/or refracted phases provide unique sampling in each layer as depicted in Figure 5. Three velocity interfaces serve as depth dividers. An upper crust veneer (0.7 km) was used in calculating travel times and ray paths but was not treated as a depth interface for inversion. The velocity-defined upper crust (0-28 km, including veneer) is further divided at 15 km depth, as this is the depth extent of

shallow earthquakes and separates up-going P_g from all down-going phases. The lower crust (28 km to Moho) is additionally divided at 33 km depth to separate the refracted P_2 phase from other down-going phases. The upper mantle is sampled by both P_n refracted phases from shallow events and up-going P waves from deep events and is not further divided. Horizontal grid nodes were spaced at 25 km to capture lateral variations in attenuation based on resolution capabilities.

The path integrated t^* values are mapped into each cell based on the amount of travel time a ray spends in each cell it traverses, which is a product of the distance traveled and velocity (Equation 2). Earthquakes were located using the Monigle et al. [2012] 1D velocity model (Figure 5), which was extrapolated throughout the study region and used to determine planar ray paths. Earthquake locations and modeled ray paths were assessed using the same model, providing self-consistent data. The modeled travel times as compared to the observed travel times have a mean residual of 0.1 second (standard deviation: 0.95s). After travel time has been calculated for each ray in all cells, a damped and smoothed least squares inversion was implemented to assess the Q structure.

Throughout the region we observe both up-going and down-going P phases. In the case of up-going P_g, all t^* attenuation is mapped into the uppermost crust layer. In the case of down-going phases and those from deep earthquakes, the rays are traced through each layer and attenuation is parsed accordingly. As a result of the diversity of up-going and down-going P phases, we are able to identify the Q_p structure in all depth layers individually. As S phases are only observed as up-going S_g from shallow

earthquakes and up-going rays from deep events, we are unable to uniquely identify the Q_s structure in each individual layer. Instead, we directly invert for the Q_s structure of the uppermost crust (0-15 km) using shallow S_g phases. As we are most interested in the attenuation structure of the middle and lower crust for imaging partial melt, we correct deep *S*-wave t^* values to isolate the 15 km to Moho structure. To do this, we correct the deep *S*-wave t^* values for travel through the upper crust Q_s structure and a range of scaled mantle Q_p structures (Q_p/Q_s =[1.0, 1.5, 2.25]) to evaluate a range of probable Q_s in the middle and lower crust, treated as a single layer. We apply the same technique for deep *P* wave t^* values to generate a Q_p/Q_s ratio of the middle and lower crust that is later used to create Q_s transects.

To test the robustness of the results and the ability to resolve lateral variation, data are forward modeled based on the predicted ray distribution of this study. Error in the ray path is not considered as travel time residuals are low, approximately normally distributed, and greater error is likely associated with calculating the source and attenuation from spectra. We test the ability to resolve depth variation using t^* data generated for a representative 1D attenuation model. Data (t^*) are perturbed with normally distributed noise varying up to 20% and inverted, reproducing the starting model within error indicating minimal tradeoff between depth layers. Additional t^* data are generated for a checkerboard style 3D attenuation model to determine our ability to resolve lateral variation with depth. Results are shown in Supplemental Figures S1-S4 and show regions of smearing and reduced resolution around the periphery of the array. Throughout the region, we are able to uniformly resolve

features on the order of 50 km, with the exception of the P_2 refracted layer (Layer 3: 28-33 km depth) where it is difficult to observe fine scale structure. In the upper crust, we are able to resolve features on the order of 25 km due to increased ray density. In particular, the region encompassed by Profile A is well resolved for both Q_p and Q_s, with near complete model recovery, while profile B is only well resolved for the Q_p structure. It is important to note that with depth, the scale of features resolvable in our study exceeds the scale of features observed in our results.

1.5 Results

Table 1 shows results for a 1D inversion to examine attenuation with depth, not considering lateral variability. Error (1σ) was estimated based on model resolution and covariance of t^* data and is generally near 10%, which is consistent with other t^* attenuation studies [e.g. Sarker and Abers, 1999]. The results suggest *P* wave energy is moderately attenuated within the uppermost 33 km. *S* wave energy, comparatively, is less attenuating in the upper 15 km (Q_s~500) where a direct comparison can be made. As a whole, the lower crust below 33 km is the most attenuating, with a bulk Q_p=250, and the mantle is less attenuating as a whole than both the upper and lower crust. Deep events provide *S* attenuation from the mantle to the surface, but the absence of down-going *S* rays from the upper crust limits the ability to directly calculate *S* attenuation for individual layers at depth. As a result, interpretation of the results at depth will be

largely based on *P*-wave observations. Expanding the inversion to 3D reduces the residual by nearly half, indicating the importance of lateral variations in the region.

While 1D results are important to understand the behavior of seismic energy as it traverses the entirety of the Tibetan plateau, smaller-scale variability in attenuation is important to understand and interpret the tectonic structure within the plateau. Attenuation in the upper crust (Figures 8,9) has three zones approximately associated with known geologic terranes. To the south, the Himalaya has moderate Q_p ($300 \lesssim Q \lesssim 400$) near the upper crustal 1D values (Figure 8). The region associated with the Lhasa terrane has low attenuation ($Q \gtrsim 450$), while the Qiangtang terrane exhibits uniformly high attenuation ($Q \lesssim 250$). *P*-wave attenuation reveals decreased Q bands approximately collocated with graben structures and alternating bands of higher Q_p. Strike-slip faulting farther north is also marked by decreased Q in the upper crust and appears to make the transition between the Lhasa and Qiangtang terrane 100 km south of the BNS. The disparity between Q_p and Q_s in the uppermost crust, where the Q_p/Q_s ratio is almost uniformly less than one (Figure 10) indicates that shear waves propagate more efficiently and may be a result of the aqueous fluid saturation state, which may be further supported by systematic changes in attenuation with takeoff angle from shallow events (Figure 11).

At depth, the attenuation structure seems to be controlled by the SIP. Figure 12 shows the upper mantle Q_p structure, where the termination of the Indian mantle is marked by a sharp transition from high to low Q material near 400 km (~31° N). Figures 13 and Figure 14 show attenuation transects A-A’ and B-B’ for Q_p and A-A’

for Q_s, respectively. Q_s transects in Figure 14 are based on three potential mantle Q_p/Q_s ratios and are generated scaling the Q_p transect between 15 km and the Moho by the Q_p/Q_s ratio established using only data from deep events. Increasing the Q_p/Q_s ratio of the mantle in deep *S* attenuation analysis effectively shifts more attenuating material from the lower crust into the mantle. The lower crust is almost uniformly low *Q* with high *Q* bodies just north of the termination of the SIP and particularly high attenuation observed immediately above the SIP, where Q_p approaches ~150 and Q_s may approach ~100.

A tectonic interpretation of the results is shown in Figure 15, where the attenuation results of this study have been draped over the receiver function tectonic model of Nabelek et al. [2009]. It is important to note that our velocity model does not account for Moho topography. In the south (<250 km from MFT), where the Moho is sloping downward, we may be underestimating the *Q* values in the lower crust due to the high *Q* SIP mantle. The Moho step to the north under the Qiangtang block is unlikely to affect our lower crust results as each is similarly highly attenuating. The attenuation results clearly show the BNS and YTS are not associated with any transition in the upper or lower crust and are therefore not likely to be active boundaries. Sharp transitions in attenuation structure coincident with strike-slip faulting in the upper crust and the termination of the SIP in the lower crust and mantle may indicate faulting through the entire crust and upper mantle. This may mark the separation of Eurasian derived material to the north from that of the SIP and overlying Tibetan crust to the south through a zone of strike-slip faulting.

1.6 Discussion

1.6.1 Aqueous fluids

We observe that shear waves are able to propagate more efficiently in the upper crust than compressional waves, as the Q_p/Q_s ratio is almost uniformly less than one above 15 km depth (Figure 10). Below 15 km, we observe compressional wave attenuation is reduced, while shear wave attenuation may be enhanced. These results suggest that the uppermost crust, to 15 km depth, is partially saturated with aqueous fluids and full fluid saturation is achieved between 15-28 km depth (Figure 15).

For standard dry rock, assuming a Poisson solid and negligible contribution of bulk attenuation, shear attenuation should be 2.25 times greater (lower Q) than compressional attenuation ($Q_\alpha^{-1} \approx (4/3)(\beta/\alpha)^2 Q_\beta^{-1}$). Toksoz et al. [1979] demonstrated that at ultrasonic frequencies, partial fluid saturation resulted in $Q_p/Q_s<1$ at high and low pressures. This was similarly documented in the upper crust in southern California [Abercrombie, 1995; Hauksson and Shearer, 2006] with a Q_p/Q_s ratio nearly identical to this study, and additionally in the Himalaya block of the Sheehan et al. [2013] study, though it was not explicitly addressed. As saturation increases, an increase in both shear (Q_s) and compressional (Q_p) attenuation is observed as liquid can flow in response to crack dilation and compression [Winkler and Nur, 1979]. At full aqueous saturation, compressional attenuation is reduced because flow parallel to propagation is impeded; shear attenuation continues to

increase because fluid "squirting" is able occur between cracks of different orientation or aspect ratio to the passing wave. This is consistent with Toksoz et al. [1979] experimental results, where Q_p was 10-25% larger (less attenuating) than Q_s for fully saturated material, and consistent with Q_p observations below 15 km in this study.

Fluid saturation at depths below 15-25 km is consistent with MT observations where widespread highly conductive material has been imaged under the plateau [Wei et al., 2001; Unsworth et al., 2005], coincident with seismic reflectors [Nelson et al., 1996] and receiver function LVZs [Nabelek et al., 2009], which also coincide with our zone of inferred fluid saturation (Figure 15). The high conductivity values can be explained by a 1.6 km thick layer containing 10% connected aqueous brine, a 16 km thick layer containing 10% partial melt, or a combination of both aqueous fluid and melt [Wei et al., 2001]. A thick layer of partial melt is unlikely in the upper crust, as we observe high Q_p between 15-30 km depth and a ubiquitous low-to-normal V_p/V_s ratio throughout the upper crust [Riddle et al., 2014b, High Resolution Regional Travel-Time Tomography in South-Central Tibet: Imaging Tibetan Crust Beneath the Hi-CLIMB Array, manuscript in preparation]. A narrow layer of connected aqueous fluids is consistent with a conservative interpretation of the INDEPTH reflectors [Makovsky and Klemperer, 1999] and the resulting narrow band of high shear attenuation could also explain the apparent blocking of down-going S-phases from shallow events observed in this study.

The interpretation of partial and full aqueous fluid saturation is broadly consistent with other attenuation studies in Tibet. Results from INDEPTH L_g

attenuation studies [Xie, 2002, Xie et al., 2004] indicate severe attenuation in the Lhasa terrane, which is expected if the waveguide includes the fully saturated crust. In the Himalaya, the Sheehan et al. [2014] Q results are also consistent, though their interpretation differs in some cases, as we do not consider $Q \approx 500$ to be high attenuation. Upper crust attenuation results imply the movement of fluids within cracks and pore space has a strong control on the observed attenuation. This may be further indicated by systematic changes in path-averaged attenuation with takeoff angle from shallow events (Figure 11). Figure 11 shows path-average attenuation for *S*-waves from rays associated with four, well-located, shallow events. *P*-waves exhibit similar patterns (not shown). Events E1, E2, and E4 show evidence of attenuation decreasing as the takeoff angle becomes more horizontal, even in the case of E4, which is located in a low Q zone (Figure 9). Event E3, however, does not have near-vertical takeoff angles and all rays exhibit high Q. If this is the result of aqueous fluid motion and squirting, attenuation may provide some indication of fracture intensity and/or orientation, where near vertical ray paths in this case are more susceptible to driving fluid motion and therefore are more attenuated. With this data set, it is difficult to invoke this process conclusively without a thorough understanding of the local fracture networks. As lateral variations in attenuation are observed to overprint the takeoff angle relation, this is unlikely to be responsible for the observed trends. Compaction and the closure of cracks is likely to play a role in this process, however, it is difficult to access its importance.

1.6.2 Faulting and tectonics

Figure 1 shows major faulting trends in the region: north-south trending graben structures extend across the YTS and into the Lhasa terrane and terminate at east-west strike-slip faulting south of the BNS. In the region straddling the YTS, decreased Q_p bands are approximately collocated with graben structures and attenuation anomalies range 25-75 km width with alternating bands of higher Q_p (Figure 13B). The topographic expression of grabens typically ranges 10-25 km, which is at the resolution threshold of the uppermost crust in this study. As a result, it is not possible to resolve each N-S graben structure independently and not all grabens are associated with decreased Q. Our results additionally do not show evidence of low Q_p below 15 km depth in the upper crust (Figure 13C), though this is may be due to a reduction in resolution below 15 km.

Given the inferred aqueous fluid saturation state of the upper crust and no observed increase in the Q_p/Q_s ratio in the region of normal faulting (Figure 10), increased fluid presence or pressure is unlikely to explain the observed increase in attenuation. Additionally, the graben anomalies are unlikely to be associated with increased heat flow, as the Qiangtang terrane exhibits lower Q than any graben (Figure 8), including a region associated with geysering along the main array near the YTS. A similar observation is made in southern California, where attenuation is sometimes discordant with heat flow [Hauksson and Shearer, 2006]. Given our reduced resolution below 15 km depth, it is possible that we are not able to resolve increased heat or fluids associated with individual grabens at depth. However, with ~50 km spacing

between grabens, uniformly low Q might be expected below this region, which is not observed. As a result, anomalous low Q_p associated with normal faulting is likely the result of well-formed basin structures that do not extend below 15 km depth. While the attenuation signal of the grabens is likely superficial, these results do not preclude normal faults extending below 15 km depth in southern Tibet, as this is clearly beyond our resolving power.

Transform faulting near the BNS, however, exhibits high attenuation through the upper crust (to 28 km depth), effectively ending the low attenuation of the Lhasa terrane 100 km south of the BNS (Figure 13A). In this region, it is possible that low $Q_{p,s}$ is the result of increased fluid pressure in the upper crust, as there is an LVZ [Nabelek et al., 2009; Riddle, 2014b] and evidence of $Q_p/Q_s>1$ in the local vicinity of Profile A, though not along the entire strike-slip boundary (Figure 10). High Q_p/Q_s was observed along the San Jacinto fault in southern California in a region otherwise dominated by $Q_p/Q_s<1$ and interpreted to be a result of decreased shear strength through high fluid pressure or full fluid saturation [Hauksson and Shearer, 2006]. Eberhart-Phillips et al. [2005] similarly image a low Q_p strike-slip fault zone as a potential fluid pathway, though interaction of this fault zone with the hydrated subducting plate complicates a direct comparison.

Several observations indicate that there are compositional changes throughout the crust and upper mantle coincident with the termination of the SIP at depth. In the upper mantle (Figure 12), we observe a sharp transition from high Q, in some cases $Q_p>1000$, to $Q_p<250$ over a short distance. High upper mantle attenuation under the

Qiangtang terrane was previously documented by Barazangi and Ni [1982], where S_n phases crossing this region are blocked. This transition is coincident with sharp transitions from higher to lower mantle V_p (8.5 to 8.2 km/s) [Riddle et al., 2014b], which track the laterally sinuous nature of the observed attenuation transition. There is evidence from deep events of a sharp attenuation contrast from low to high Q_p through the middle and lower crust (15 km-Moho) coincident with this boundary; however, the Q_p structure, which includes data from shallow events is more complex with localized regions of high and low Q interrupting the broad scale structure. Additionally, discontinuous high $Q_{p,s}$ bodies interrupt the dominantly low $Q_{p,s}$ lower crust (33 km-Moho) immediately north of the SIP termination (Figure 13, 14).

The sharp attenuation transitions in the upper crust and upper mantle change from high to low Q to the north, while the lower crust exhibits the opposite transition, from low to high Q. As a result of the sharpness and alternating transitions with depth, these observations are unlikely to be related to heat, as thermal models predict laterally homogenous temperatures that increase monotonically with depth [Wang et al., 2013; Nabelek and Nabelek, 2014]. Instead, these observations more likely mark a compositional transition between materials of Indian and Eurasian descent. Velocity tomography results in the lower crust and mantle indicate material changes consistent with attenuation data, to high velocities in the lower crust and lower velocities in the mantle approaching the Qiangtang terrane from the south [Riddle et al., 2014b]. Similarly, receiver functions observe changes in fabric orientation in the upper mantle [Nabelek et al., 2009] and anisotropy patterns also illustrate a change in orientation

coincident with the termination of the SIP [Chen and Ozalaybey, 1998]. All results are consistent with lithosphere scale changes initiating at the termination of the obliquely subducting Indian plate.

1.6.3 Partial melt and mechanical implications

The attenuation structure of the upper crust (to 28 km depth) in this study is consistent with felsic material throughout the array, which is further supported by the velocity data from Riddle et al., [2014b] and southern Tibet attenuation analysis of Sheehan et al. [2013]. Accordingly, the lowest Q_p values in this area approach ~200 in faulted regions, with Q_p>400 almost universally between 15-28 km depth (Figures 12 and 13). As a result, these relatively high $Q_{p,s}$ values preclude any partial melt in the upper crust, as observed partial melt and fluid pathways in volcanic arc settings exhibit Q_p<100 [Schurr et al., 2003; Eberhard-Phillips et al., 2005].

In the lower crust (28 km to Moho) we do observe low $Q_{p,s,}$ specifically south of 31° latitude (400 km: Figure 13, 14), which may be of thermal origin as velocities in the region are relatively constant with depth until the base of the lower crust [Riddle et al., 2014b]. In this case, the presence of fluids, including partial melt, is possible at depth in the lower crust. However, as Q_p values range ~200-250 and Q_s may approach ~100, results are consistent with a thin layer of partial melt predicted by thermal models [Nabelek and Nabelek, 2014] and not extensive partial melt as may be expected in volcanic settings, which is further supported by lower crust Vp/Vs ratios no higher than 1.8 [Riddle et al., 2014b]. This observation is consistent with the

Sheehan et al. [2014] results depicting low Q at 45-50 km depth and interpreted as a small pocket of pooled aqueous fluids or melt.

Under the assumption that seismic bright spots and MT data represent partial melt at 15-25 km depth in the upper crust [Nelson et al., 1996; Unsworth et al., 2005], channel flow models have been proposed to explain the outward growth of the Tibetan plateau. Channel flow models propose ductile extrusion along low-viscosity channels in the crust, which rely on high heat production in the upper crust and partial melt throughout the Tibetan plateau [Beaumont et al., 2001; Beaumont et al., 2004; Klemperer, 2006]. These models have been supported by seismic data showing evidence for LVZs at various depths in the crust in the Lhasa and Qiangtang terranes: 20-40 km [Rapine et al., 2003], 30-50 km [Kind et al., 1996], or 30-70 km depth [Cotte et al., 1999]. MT results, however, reveal high conductivity zones in the Himalaya and Lhasa terrane at depths ranging 15-25 km, and increasing in depth beginning near 31° N to 40-50 km under the Qiangtang terrane in the vicinity of this study [Wei et al., 2001]. These attenuation results are also inconsistent with a low-viscosity channel between 20-30 km in the upper crust, as experimental data for the deformation of partially melted granite indicates 3-7% partial melt is required for interconnected melt pathways and a significant decrease in strength [Rosenberg and Handy, 2005]. At this percentage, the layer of partial melt would need to be greater than 15 km thick to match the MT signature [Wei et al., 2001] in southern Tibet, which is well within the resolution range of this study. We cannot rule out lower viscosity material in the lower crust, where we do observe increased attenuation.

However, our interpretation narrow zones of partial melt near the base of the lower crust are inconsistent with extensive zones of partial melt in the middle and lower crust [e.g. Klemperer, 2006] and would imply that channel flow models may not be appropriate to explain plateau development and expansion. Instead, models that predict mechanical coupling may be more appropriate, which specifically preclude a low-viscosity channel in the crust.

The attenuation transitions coincident with the termination of the SIP and upper crust strike-slip faulting likely indicates that faulting extends from the Moho through the entirety of the Tibetan crust (Figure 15). This indicates stress transfer between the upper mantle and upper crust and a shift from extensional stress above the SIP to translational stress at the termination of subduction. These observations are consistent with a mechanical coupling model to explain deformation in Tibet, in which the oblique subduction of the Indian plate beneath Tibet generates basal drag, which in turn influences faulting in the upper crust [McCaffrey and Nabelek, 1998]. Numerical modeling [Copley et al., 2011] requires a rigid lower crust to couple shear stress to the overlying material and results in normal faulting in southern Tibet, which overlies the SIP, and strike-slip motion north of the termination of the subducting plate. In the case of a weak or decoupled lower crust, observed normal faulting is not reproduced. While our results do not unequivocally support mechanical coupling models for deformation, we do not find significant evidence for widespread partial melt in the Tibetan upper crust, which suggests channel flow models may not be appropriate.

1.7 Summary and Conclusions

Attenuation results indicate high *Q* material in the upper crust of the Himalaya and Lhasa blocks, which is cut by shallow extensional graben structures in southern Tibet and terminates with the initiation of strike-slip faulting south of the BNS, where faulting penetrate to at least 30 km depth. The attenuation structure in the upper crust strongly implies increasing aqueous fluid content with depth, reaching full saturation between 15-30 km and possibly blocking down-going *S*-waves from shallow earthquakes. The low attenuation signature of the subducting India plate upper mantle is clearly visible to 400 km north of the MFT, with a sharp transition to high attenuation upper mantle associated with the Eurasian plate and Qiangtang terrane. This sharp transition is marked in the otherwise ubiquitously high attenuation lower crust by low attenuation bodies, which cannot by explained by the thermal structure. There may be evidence of partial melt in the lower crust above the SIP. The sharp attenuation transitions through the crust and upper mantle suggest strike-slip motion is occurring along a lithosphere scale boundary, separating SIP and Tibetan crustal material to the south, from Eurasian material to the north.

1.8 References

Abercrombie, R. E. [1995], Earthquake source scaling relationships from −1 to 5 M_L using seismograms recorded at 2.5-km depth, *J. Geophys. Res.*, *100*(B12), 24015–24036, doi:10.1029/95JB02397.

Aki K, and P.G. Richards [1980], *Quantitative Seismology: Theory and Methods*, W.H. Freeman and Company, San Francisco, Calif.

Bao, X., E. Sandvol, J. Ni, T. Hearn, Y.J. Chen, and Y. Shen [2011], High resolution regional seismic attenuation tomography in eastern Tibetan Plateau and adjacent regions, *Geophys. Res. Lett., 38*, L16304, doi: 10.1029/2011GL048012.

Barazangi, M. and J. Ni [1982], Velocities and propagation characteristics of Pn and Sn beneath the Himalaya arc and Tibetan plateau: Possible evidence for underthrusting of Indian continental lithosphere beneath Tibet, *Geology*, *10*, 179-185.

Baur, J [2007], Seismotectonic analysis of the Himalaya-Tibetan collision zone from regional seismic moment tensor analysis with Hi-CLIMB data, *MS Thesis*, *Oregon State Univ.*, Corvallis, Oregon, 276 pp.

Beaumont, C., R. A. Jamieson, M. H. Nguyen and B. Lee [2001], Himalayan tectonics explained by extrusion of a low-viscosity crustal channel coupled to focused surface denudation, *Nature, 414,* 738-742, doi:10.1038/414738a.

Beaumont, C., R. A. Jamieson, M. H. Nguyen, and S. Medvedev [2004], Crustal channel flows: 1. Numerical models with applications to the tectonics of the Himalayan-Tibetan orogen, *J. Geophys. Res.*, *109*, B06406, doi:10.1029/2003JB002809.

Bouchon, M. (1982), The complete synthesis of seismic crustal phases at regional distances, *J. Geophys. Res*., *87*(B3), 1735–1741, doi: 10.1029/JB087iB03

Carpenter, S [2010], South-Central Tibetan Seismicity Recorded by HiCLIMB Seismic Array, M.S. thesis, 248 pp., Oregon State Univ., Corvallis, 4 October.

Chen, W. P., and S. Ozalaybey [1998], Correlation between seismic anisotropy and Bouguer gravity anomalies in Tibet and its implications for lithospheric structures. *Geophys. J. Int.*, *135*(1), 93-101.

Copley, A., J.-P. Avouac, and J.-Y. Royer [2010], India-Asia collision and the Cenozoic slowdown of the Indian plate: Implications for the forces driving plate motions, *J. Geophys. Res.*, *115*, B03410, doi:10.1029/2009JB006634.

Copley, A., Avouac, J.-P. & Wernicke, B.P., [2011]. Evidence for mechanical coupling and strong Indian lower crust beneath southern Tibet, *Nature, 472***,** doi:10.1038/nature09926.

Cotte, N., H. Pedersen, M. Campillo, J. Mars, J.F. Ni, R. Kind, E. Sadvol, and W. Zhao [1999], Determination of the crustal structure in southern Tibet by dispersion and amplitude analysis of Rayleigh waves, *Geophys. J. Int.*, *138*, 809-819.

Eberhart-Phillips, D., M. Reyners, M. Chadwick, and G. Stuart [2005], Three-dimensional attenuation structure of the Hikurangi subduction zone in the central North Island, New Zealand, *Geophys. J. Int.*, *174*(1), 418-434, doi:10.1111/j.1365-246X.2008.03816.x

Fisk M.D., and W.S. Phillips [2013], Constraining Regional Phase Amplitude Models for Eurasia, Part 1: Accurate Source Parameters and Geometric Spreading, *Bull. Seis. Soc. Am.*, *103*(6), 3248-3264, doi:10.1785/0120130018.

Ford, S.R., D.S. Dreger, K. Mayeda, W.R. Walter, L. Malagnini, and W.S. Phillips [2008], Regional Attenuation in Northern California: A Comparison of Five 1D Q Methods, *Bull. Seis. Soc. Am., 98*(4), 2033-2046, doi: 10.1785/0120070218.

Haberland, C., and A. Rietbrock [2001], Attenuation tomography in the western central Andes: A detailed insight into the structure of a magmatic arc, *J. Geophys. Res*., *106*(B6), 11151–11167, doi:10.1029/2000JB00472

Hartse, H.E., S.R. Taylor, W.W. Phillips, and G.E. Randall [1997], A preliminary study of regional seismic discrimination in central Asia with emphasis on western China, *Bull. Seism. Soc. Am., 87*, 551-568.

Hauksson, E., and P. M. Shearer [2006], Attenuation models (Q_P and Q_S) in three dimensions of the southern California crust: Inferred fluid saturation at seismogenic depths, *J. Geophys. Res*., *111*, B05302, doi:10.1029/2005JB003947.

Jackson, I. [2013] Laboratory Measurement of Seismic Wave Dispersion and Attenuation: Recent Progress, in Earth's Deep Interior: Mineral Physics and Tomography From the Atomic to the Global Scale (eds S.-I. Karato, A. Forte, R. Liebermann, G. Masters and L. Stixrude), American Geophysical Union, Washington, D. C.. doi: 10.1029/GM117p0265

Jackson, I., J. D. Fitz Gerald, U. H. Faul, and B. H. Tan [2002], Grain-size-sensitive seismic wave attenuation in polycrystalline olivine, *J. Geophys. Res*., *107*(B12), 2360, doi:10.1029/2001JB001225.

Kind, R., *et al.* [1996], Evidence from Earthquake Data for a Partially Molten Crust Layer in Southern Tibet, *Science*, *274*, 1692-1694.

Kind, R. *et al.* [2002], Seismic Images of Crust and Upper Mantle Beneath Tibet: Evidence for Eurasian Plate Subduction, *Science*, *298*(5596), 1219-1221, doi: 10.1126/science.1078115.

Klemperer, S. L. [2006], Crustal flow in Tibet: Geophysical evidence for the physical state of Tibetan lithosphere, and inferred patterns of active flow, in "Channel Flow, Ductile Extrusion and Exhumation in Continental Collision Zones", edited by R. D. Law, M. P. Searle, and L. Godin, Geol. Soc. London Spec. Publ., 268, 39–70.

Makovsky, Y., and S. L. Klemperer [1999], Measuring the seismic properties of Tibetan bright spots: Evidence for free aqueous fluids in the Tibetan middle crust, *J. Geophys. Res.*, *104*, 10,795–10,825, doi:10.1029/1998JB900074.

Mavko, G. M. [1980], Velocity and attenuation in partially molten rocks, *J. Geophys. Res.*, *85* (B10), 5173–5189, doi:10.1029/JB085iB10p05173.

McCaffrey, R. & Nabelek, J., [1998], Role of oblique convergence in the active deformation of the Himalayas and southern Tibet plateau, *Geology, 26***,** 691–694.

McCarthy, C., and Y. Takei [2011], Anelasticity and viscosity of partially molten rock analogue: Toward seismic detection of small quantities of melt, *Geophys. Res. Lett*., *38*, L18306, doi:10.1029/2011GL048776.

Mitchell, B.J. [1995], Anelastic structure and evolution of the continental crust and upper mantle from seismic surface wave attenuation, *Rev. Geophys., 33*, 441-462.

Molnar, P. [1984], Structure and tectonics of the Himalaya: Constraints and implications of geophysical data, *Annu. Rev. Earth Planet. Sci*., *12*, 489–518.

Molnar, P., and P. Tapponnier [1975], Cenozoic tectonics of Asia: effects of a continental collision. *Science*, *189* (4201), 419-426.

Monigle, P. W., J. Nabelek, J. Braunmiller, and N.S. Carpenter [2012], Evidence for low-angle normal faulting in the Pumqu-Xianza Rift, Tibet. *Geophys. J. Int.*, *190* (3), 1335-1340.

Nabelek, J. *et al.* [2009], Underplating in the Himalaya-Tibet collision zone revealed by the Hi-CLIMB experiment, *Science, 325*, 1371–1374.

Nabelek, J.L., J. Braunmiller, P. Monigle, N. Carpenter, W. Phillips [2011], Source and path calibration in regions of poor crustal propagation using temporary,

large-aperture, high-resolution seismic arrays. In: 2011 Monitoring Research Review, Ground-Based Nuclear Explosion Monitoring Technologies.

Nabelek, P.I., and J.L. Nabelek [2014], Thermal characteristics of the Main Himalaya Thrust and the Indian lower crust with implications for crustal rheology and partial melting in the Himalaya orogeny, *Earth Planet. Sci*. *Lett.*, *395*, 116-123, doi: 10.10016/j.epsl.2014.03.026.

Nelson, K. D., et al. [1996], Partially molten middle crust beneath southern Tibet: Synthesis of project INDEPTH results, *Science*, *274*(5293), 1684–1688.

Rapine, R., F. Tilmann, M. West, J. Ni, and A. Rodgers [2003], Crustal structure of northern and southern Tibet from surface wave dispersion analysis, *J. Geophys. Res.*, *108*(B2), 2120, doi: 10.1029/2001JB000445.

Riddle, E., J. Nabelek, and J. Braunmiller, [2014a]. Implementation of an Automatic Polarization *S* wave Picker for Local Earthquake Tomography in South-Central Tibet. Manuscript in preparation.

Riddle, E., J. Nabelek, and J. Braunmiller, [2014b]. High Resolution Regional Travel-Time Tomography in South-Central Tibet: Imaging Tibetan Crust Beneath the Hi-CLIMB Array. Manuscript in preparation.

Rosenberg, C. L., and M.R. Handy [2005], Experimental deformation of partially melted granite revisited: implications for the continental crust. *J. Metamorphic Geol.*, *23*(1), 19-28.

Ruddiman, W.F., and J.E. Kutzbach [1989], Forcing of late Cenozoic northern hemisphere climate by plateau uplift in southern Asia and the American West. *J. Geophys. Res.*, *94*(D15), 18409-18427.

Sarker, G., and G.A. Abers [1999], Lithospheric temperature estimates from seismic attenuation across range fronts in southern and central Eurasia. *Geology*, *27*(5), 427-430.

Schurr, B., G. Asch, A. Rietbrock, R. Trumbull, and C.H. Haberland [2003], Complex patterns of fluid and melt transport in the central Andean subduction zone revealed by attenuation tomography. *Earth and Plan. Sci. Lett.*, *215*(1), 105-119.

Shearer, P. M., Prieto, G. A., & Hauksson, E. (2006). Comprehensive analysis of earthquake source spectra in southern California. *J. Geophys. Res.*, *111*(B6) doi:10.1029/2005JB003979

Sheehan, A. F., T. L. de la Torre, G. Monsalve, G. A. Abers, and B. R. Hacker (2014), Physical state of Himalayan crust and uppermost mantle: Constraints from seismic attenuation and velocity tomography, *J. Geophys. Res.,* 119, 567–580, doi:10.1002/2013JB010601.

Stein, S., and M. Wysession [2003], *An Introduction to Seismology, Earthquakes, and Earth Structure*, Blackwell Publishing, Malden, Mass.

Toksoz M.N., D.H. Johnson, and A. Timur [1979], Attenuation of seismic waves in dry and saturated rocks: I. Laboratory measurements, *Geophys.*, *44*(4), 681-690, doi: 10.1190/1.1440969.

Unsworth, M. J., A. G. Jones, W. Wei, G. Marquis, S. G. Gokarn, and J. E. Spratt [2005], Crustal rheology of the Himalaya and southern Tibet inferred from magnetotelluric data, *Nature*, *438*(7064), 78–81.

Wang, C. Y., W. P. Chen, and L. P. Wang [2013], Temperature beneath Tibet, *Earth Planet. Sci. Lett.*, *375*, 326–337, doi:10.1016/j.epsl.2013.05.052.

Wei W., *et al.* [2001], Detection of Widespread Fluids in the Tibetan Crust by Magnetotelluric Studies, *Science*, *292*(5517), 716-719, doi: 10.1126/science.1010580

Winkler, K. W., and A. Nur (1979), Pore fluids and seismic attenuation in rocks, *Geophys. Res. Lett*., *6*, 1–4.

Xie, J., R. Gok, J. Ni, and Y. Aoki [2004] Lateral variations of crustal seismic attenuation along the INDEPTH profiles in Tibet from *Lg Q* inversion, *J. Geophys. Res., 109*, B10308, doi:10.1029/2004JB002988.

Xie, J. [2002], *Lg Q* in the eastern Tibetan Plateau, *Bull. Seismol. Soc. Am., 92*, 871–876.

Xie J. [2007], Pn Attenuation beneath the Tibetan plateau, *Bull. Seismol. Soc. Am., 97,* 2040-2052, doi: 10.1785/0120070016

Yin A., and T.M. Harrison [2000], Geologic Evolution of the Himalayan-Tibetan Orogen, *An. Rev. Earth and Planet. Sci., 28,* 211-280 doi:10.1146/annurev.earth.28.1.211

Zhao, W. J., K. D. Nelson, and Project INDEPTH Team [1993], Deep seismic reflection evidence for continental underthrusting beneath southern Tibet, *Nature*, *366*(9), 557–559.

Zhu, D.C. *et al.* (2011). The Lhasa Terrane: Record of a microcontinent and its histories of drift and growth. *Earth Planet. Sci. Lett.*, *301*(1), 241-255.

1.9 Figure Captions

Figure 1. Map of the HiCLIMB array and study region. Faults in black solid lines and adapted from Yin and Harrison [2000]. Qiangtang, Lhasa, and Himalaya blocks are labeled to the right and the Bangong-Nujiang Suture (BNS), Yarlung-Tsangpo Suture (TYS) and the Main Frontal Thrust (MFT) are labeled on the left. YTS and BNS represented as dashed lines, consistent for all maps. Earthquakes shown as white circles represent catalog of events with M_L>2.5 and more than 50 identified phases. Earthquakes analyzed using SPMS ratio technique are shown as red circles, remaining analyzed earthquakes shown as green (shallow) or blue (deep) circles. Red lines represent Profiles A-A' and B-B'.

Figure 2. *P* and *S*-wave time series (A,B) and spectral data (C,D) from an M_L 3.18 earthquake recorded at 71 km epicentral distance on the same instrument (50 sps). Seismic data (black) is high-pass filtered at 0.5 Hz for plotting purposes. All spectral data are shown with amplitude range of 6 decades, consistent for all spectra figures. **A)** *P*-wave seismic data from the vertical channel showing pre-*P* noise (cyan) and signal (blue) after they have been windowed. Red 'x' is catalog arrival; red 'o' is predicted arrival. **B)** Transverse data for *S*-wave following the same color scheme and including the P_g window and catalog arrival (black 'x') for reference. **C)** *P*-wave

spectrum (blue), pre-*P* noise (cyan) and best fit model (red) for a 4.5 Hz source corner frequency (f_c), denoted with black inverted triangle. **D)** *S*-wave spectrum, noise, and fit. Both P_g and S_g spectrum are fit over entire available spectral band, 0.5-20 Hz (19.5 Hz bandwidth). Note that path integrated *Q* value for *S* spectrum is higher than for *P*, implying more efficient propagation.

Figure 3. Synthetic source corner frequency (f_c) sensitivity test for 19.5 Hz bandwidth. **A)** Synthetic spectrum with each of four source corners (5, 20, 35, and 50% Nyquist frequency) are evaluated for the best-fit attenuation at each corner (0.1-20 Hz) and the residual misfit is plotted against the Nyquist normalized corner. Synthetic spectra (inset) is shown for a 40 sps instrument at 100 km distance with a uniform Q=330 and V=6.0km/s medium. Misfit is indistinguishable for any corner ≥ 0.5 Nyquist by increasing attenuation. Best-fit *Q* values are shown at f_c =10, 15, and 20 Hz for the black 50% Nyquist source (10 Hz). **B)** The percent error of *Q* values for a 50% Nyquist source (10 Hz) vs. an indistinguishable 20 Hz source is shown for various *Q* input models (50-650) and distances (50-200 km). The error curves are solid for values within 10% of input (approximate error), with a short dash between 10-20% error (maximum acceptable), and a long dash beyond 20% error. Note: increases in bandwidth will reduce misfit error.

Figure 4. Magnitude- corner frequency relationship for events analyzed in this study. Earthquake magnitudes are calculated as in Carpenter [2010]; M_L values are assumed

to be approximately equivalent to M_w over this limited range and f_c, moment, and stress drop relationship from Shearer et al., [2006]. Data from this study are represented by blue asterisks.

Figure 5. Example of ray paths emanating from a single shallow earthquake. Layer velocities are shown on the left and velocity steps are denoted by solid lines when used as inversion depth divider ('U','L','M' are upper and lower crust, and mantle, respectively). Upper crust veneer (long-dash gray line: α_V=5.0, β_V=1.43 km/s) is a velocity step but is not used as an inversion depth divider. Short-dash lines represent additional layers used for inversion purposes. An example of each type of phase is color coded and labeled: P_g (black), upper crust interface reflection P_iP (cyan) and refraction P_2 (red), Moho reflection P_mP (magenta) and refraction Pn (blue).

Figure 6. Synthetic seismograms and resulting spectra for a Brune 4.5 Hz source f_c navigating the Monigle et al. [2012] velocity model with a uniform attenuation structure (Q=450) and recorded at 40 sps. Travel time curves shown for phases analyzed in this study. Black dash boxes in A and B are centered on the arrival and represent the time window extracted for spectra (3.4s). **A)** Record section with a 5.869 km/s reduction highlighting upper crust phases. **B)** Mantle velocity reduction (8.209 km/s) time series data highlighting Moho reflections and refractions. All subset time series data (C,D,E,F) show 4 seconds of data using color scheme as in Figure 2. **C)** Spectrum of *Pg* phase outlined in A. Recovered Q value is within error of expected.

D) Spectrum of P_iP phase. Recovered Q value is as expected. **E)** Spectrum of P_mP phase as outlined in B and recovered Q value. **F)** Spectum of P_n as analyzed in this study (blue with solid red fit) and non-differentiated spectra (black, dashed red fit), which results in over estimation of attenuation. Note pulse arrival of P_n compared to doublet shape of P_g arrival.

Figure 7. Synthetic testing of the skin depth of a P_n refracted phase at 500 km distance with a 4.5 Hz Brune source and sampled at 40sps. **A)** Q_m inversion results for various buffer layer thickness (Δ) and inset schematic of synthetic test. Crustal, non-attenuating layer (Q_c=10,000, α_c=5.869km/s) overlies non-attenuating mantle buffer layer (Q_Δ=Q_c, α_m=8.209km/s) and a high attenuation mantle half space (Q_h=100, α_m). Inverted Q_m rises sharply beyond 5 km buffer thickness. **B)** Time series waveform of refracted P_n and spectrum (blue) with modeled attenuation fit (red) for an example with no buffer layer. **C)** Example of time series and spectral data for a buffer thickness of 3 km, which exhibits hybrid waveform of non-attenuated and highly attenuated waveform. **D)** Example of the time series and spectrum with a buffer layer of infinite thickness.

Figure 8. Map view of *P*-wave attenuation structure in the uppermost crust (0-15 km). Stations indicated as yellow triangles, yellow vertical and horizontal lines represent Profiles A-A' and B-B', respectively. YTS and BNS are shown as dashed lines. All earthquakes indicated with green asterisks. Zero km (Y-axis) is referenced to the MFT

and matches Nabelek et al. [2009] receiver functions transect. Zero km (X-axis) is referenced to 86°W longitude, consistent with Riddle et al. [2014b] velocity tomography transects. Color bar for Q structure ranges 50-650, with darker red representing increasing attenuation (low Q), and darker blue representing decreasing attenuation (high Q). Neutral white colors represent moderate attenuation. Gray zones around the edges of the study area are regions of poor data coverage (See Figures S1-S4). E1-E4 are events used in Figure 11.

Figure 9. Map view of *S*-wave attenuation structure in the upper crust (0-15 km). Colors, symbols, and interpretation are the same as Figure 8. Note that Q_s is considerably greater than Q_p for the upper crust, implying shear energy is transmitted more efficiently than compressional energy.

Figure 10. Q_p/Q_s ratio in the upper crust (0-15 km). Stations, events, profile markers, and sutures are as denoted in Figure 8. Darker blue colors represent $Q_p<Q_s$ where compressional attenuation is greater than shear attenuation. Red regions represent $Q_s<Q_p$ where shear attenuation is greatest. Neutral white colors represent regions where shear and compressional attenuation are approximately equal.

Figure 11. *S*-wave path integrated attenuation as a function of takeoff angle from four well-located events (E1-E4, Figures 8,9). Inset depicts path average Q as a function of travel-time, a useful proxy for takeoff angle. In both graphs, ray paths with sub-

vertical takeoff angles, or short travel time, exhibit low Q with systematic increase in Q as takeoff angle becomes more horizontal. Event E3 does not have sub vertical ray paths and is therefore uniformly high Q. Event E4 is in a low Q region and similarly exhibits increasing Q with paths becoming more horizontal though the effect is subtler.

Figure 12. Map view of *P*-wave attenuation structure in the upper mantle (Moho-90 km). Colors and interpretation are the same as Figure 8. Note the sharp boundary between mantle attenuation to the north and south, which represents the transition from SIP mantle to Eurasia mantle.

Figure 13. Profile views of attenuation structure. Attenuation color scheme is the same as Figure 8. **A)** Profile A-A' for *P* attenuation. **B)** Represents profile B-B' for *P*-wave attenuation. 28km interface and Moho are labeled in the reduced resolution gray margins for reference. YTS and BNS are labeled where appropriate and degrees latitude are marked in A for reference. Seismic stations are shown as black triangles.

Figure 14. Profile views of *S* wave attenuation structure. Attenuation color scheme and features are the same as Figures 8 and 13. **A)** Q_s structure for mantle Q_p equivalent to mantle Q_s. This example has the lowest Q_s in the lower crust and highest Q_s in the upper mantle. **B)** Q_s structure for a mantle Q_p/Q_s ratio of 1.5. **C)** Q_s structure for a

mantle Q_p/Q_s ratio of 2.25. This example has the strongest mantle attenuation and therefore the most moderate lower crust attenuation.

Figure 15. Tectonic overview of attenuation (Q_p) draped over Nabelek et al. [2009] receiver function model of Moho (white lines), MHT (black dashed line), and LVZs (gray features). Color scheme and features identical to Figures 8 and 12. IC is the region of India upper and lower crust, TC is the Tibetan crust, and IM the Indian upper mantle. PAFS represents region of partial aqueous fluid saturation and full aqueous fluid saturation labeled as FAFS. Earthquakes analyzed in this study are shown as yellow asterisks. Dashed boxes highlight the shallow reduced Q structure of grabens and low Q upper crust strike-slip faulting (SS). Sub-vertical dashed line indicates an interpreted zone of strike-slip faulting cutting through the entire crust.

1.10 Table Captions

Table 1. Bulk 1D attenuation results. Q_p and Q_s for each of the 5 individually inverted layers without accounting for lateral variations. Q_p is directly inverted in each layer, while Q_s is only inverted directly in the uppermost crust only.

Figure 1

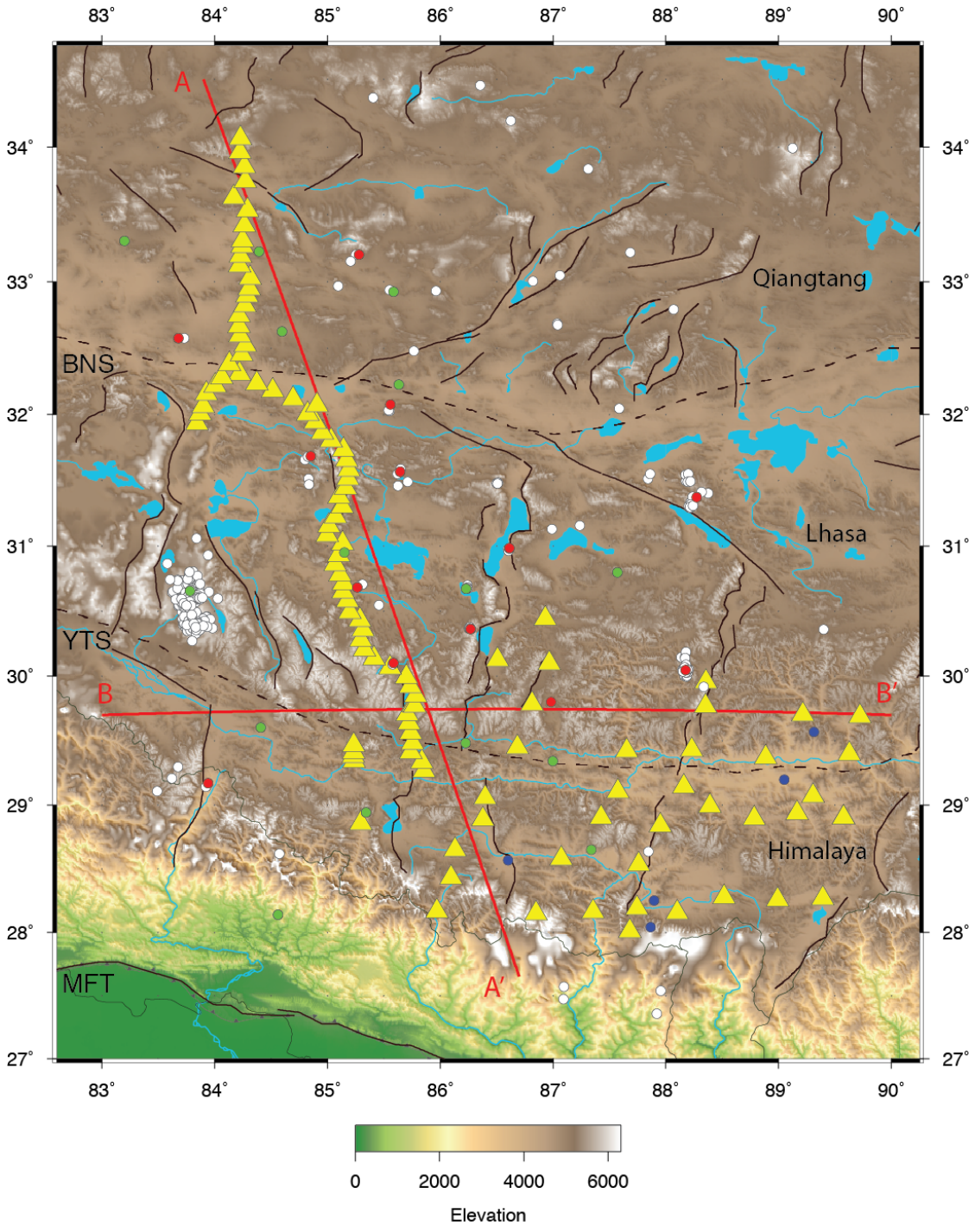
83°
84°
85°
86°
87°
88°
89°
90°
34°
33°
32°
31°
30°
29°
28°
27°
A
A′
B
B′
Qiangtang
BNS
Lhasa
YTS
Himalaya
MFT
0
2000
4000
6000
Elevation

Figure 2

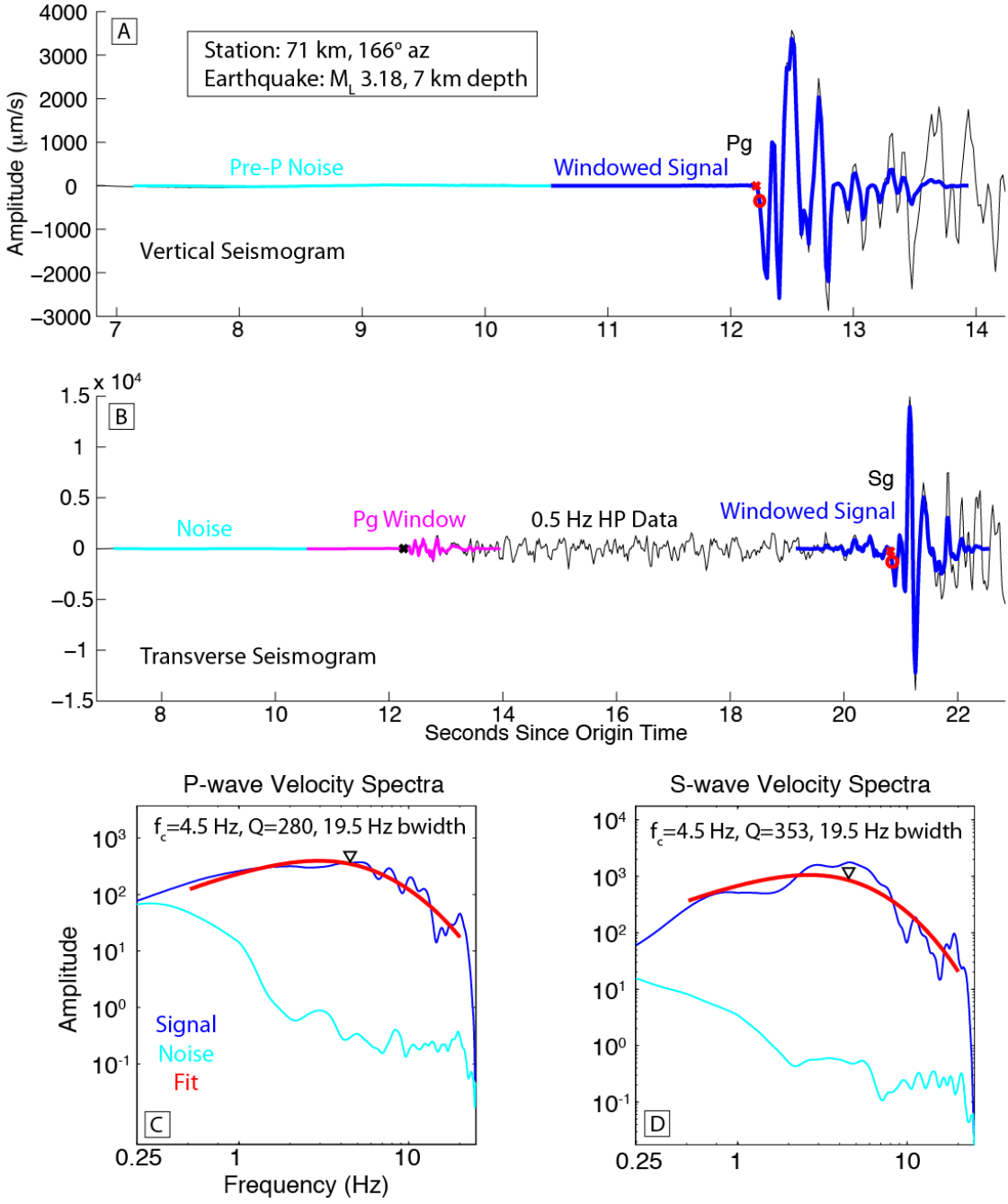
A
Station: 71 km, 166° az
Earthquake: M_L 3.18, 7 km depth
Pre-P Noise
Windowed Signal
Pg
Vertical Seismogram
Amplitude (μm/s)
B
x 10^4
Noise
Pg Window
0.5 Hz HP Data
Windowed Signal
Sg
Transverse Seismogram
Seconds Since Origin Time
P-wave Velocity Spectra
f_c=4.5 Hz, Q=280, 19.5 Hz bwidth
Signal
Noise
Fit
C
Amplitude
Frequency (Hz)
S-wave Velocity Spectra
f_c=4.5 Hz, Q=353, 19.5 Hz bwidth
D

Figure 3

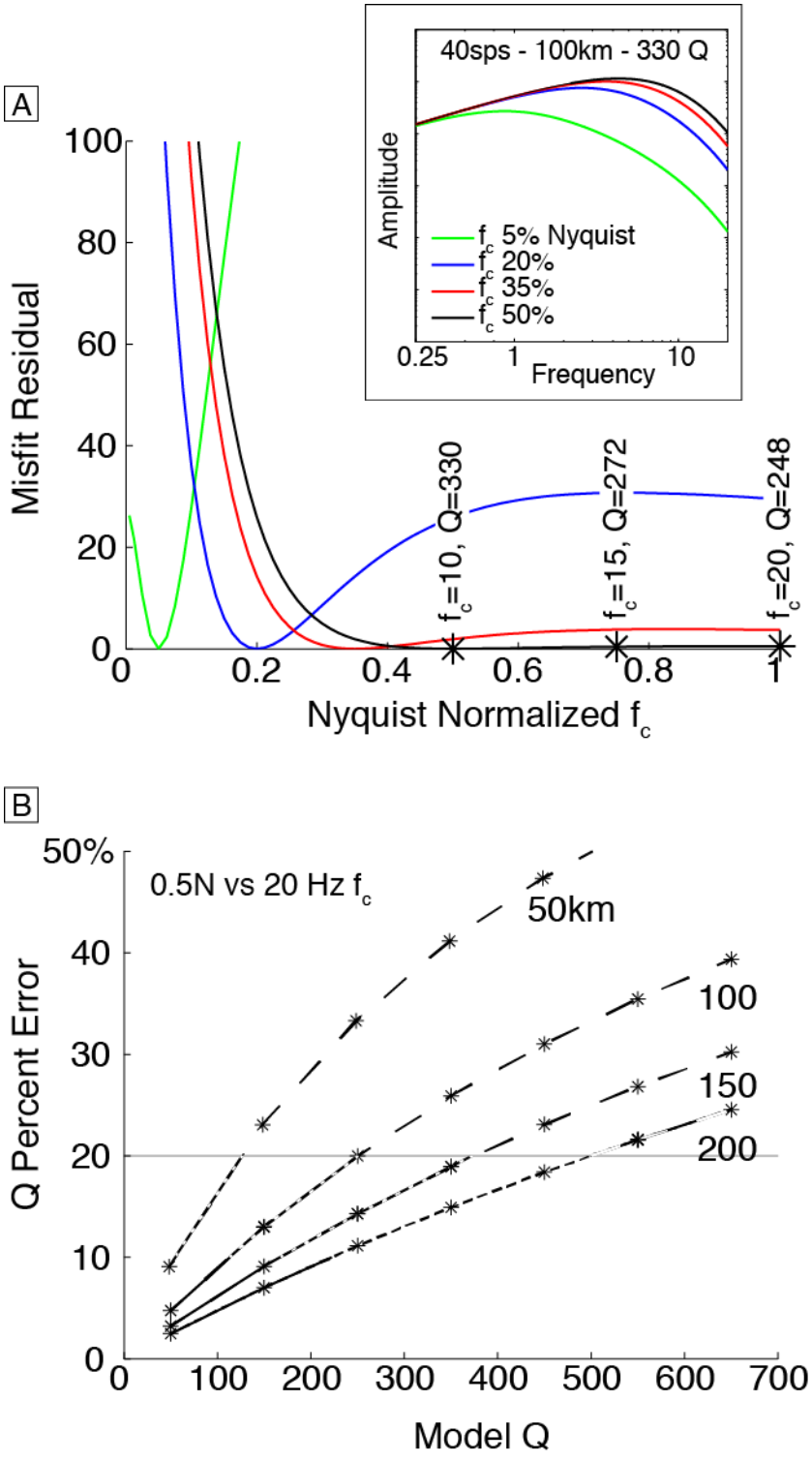
A
40sps - 100km - 330 Q
Amplitude
f_c 5% Nyquist
f_c 20%
f_c 35%
f_c 50%
0.25
1
10
Frequency
Misfit Residual
100
80
60
40
20
0
0
0.2
0.4
0.6
0.8
1
f_c=10, Q=330
f_c=15, Q=272
f_c=20, Q=248
Nyquist Normalized f_c
B
50%
0.5N vs 20 Hz f_c
50km
100
150
200
Q Percent Error
40
30
20
10
0
0
100
200
300
400
500
600
700
Model Q

Figure 4

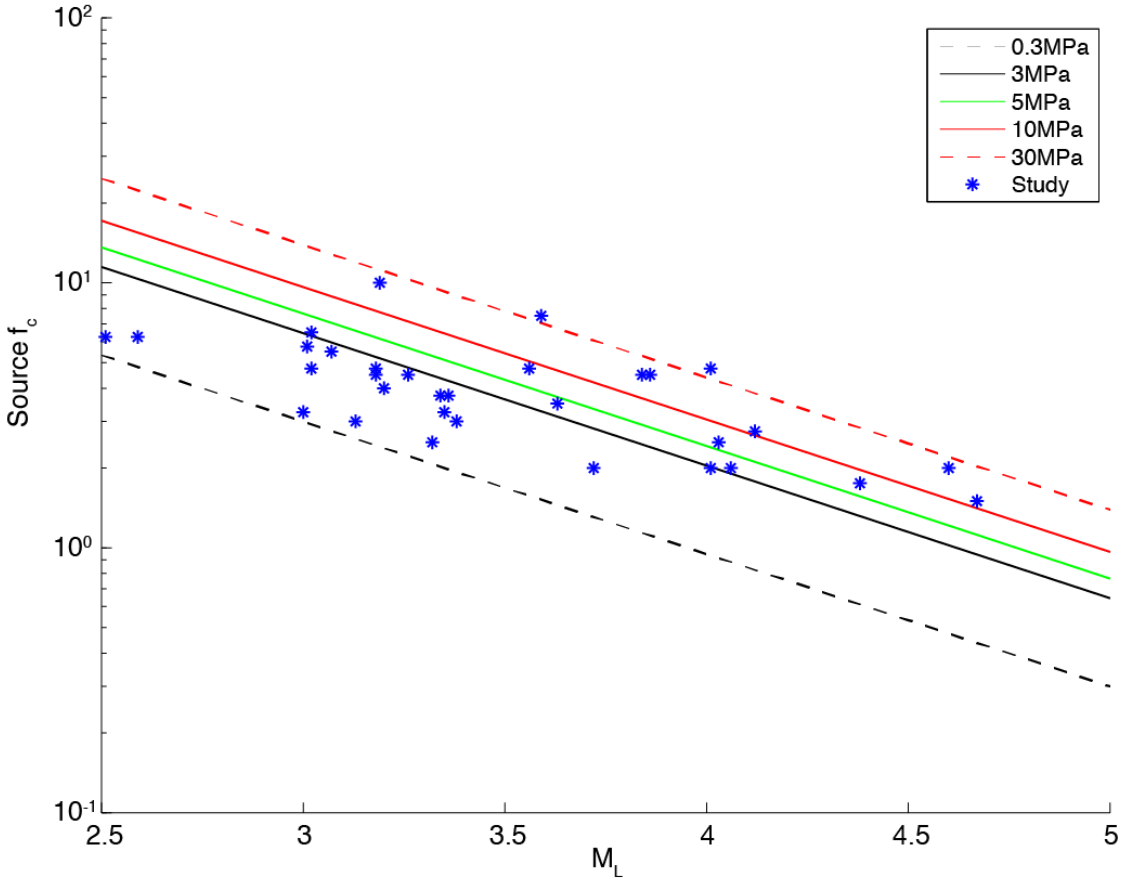
0.3MPa
3MPa
5MPa
10MPa
30MPa
Study
Source f_c
10^2
10^1
10^0
10^{-1}
2.5
3
3.5
4
4.5
5
M_L

Figure 5

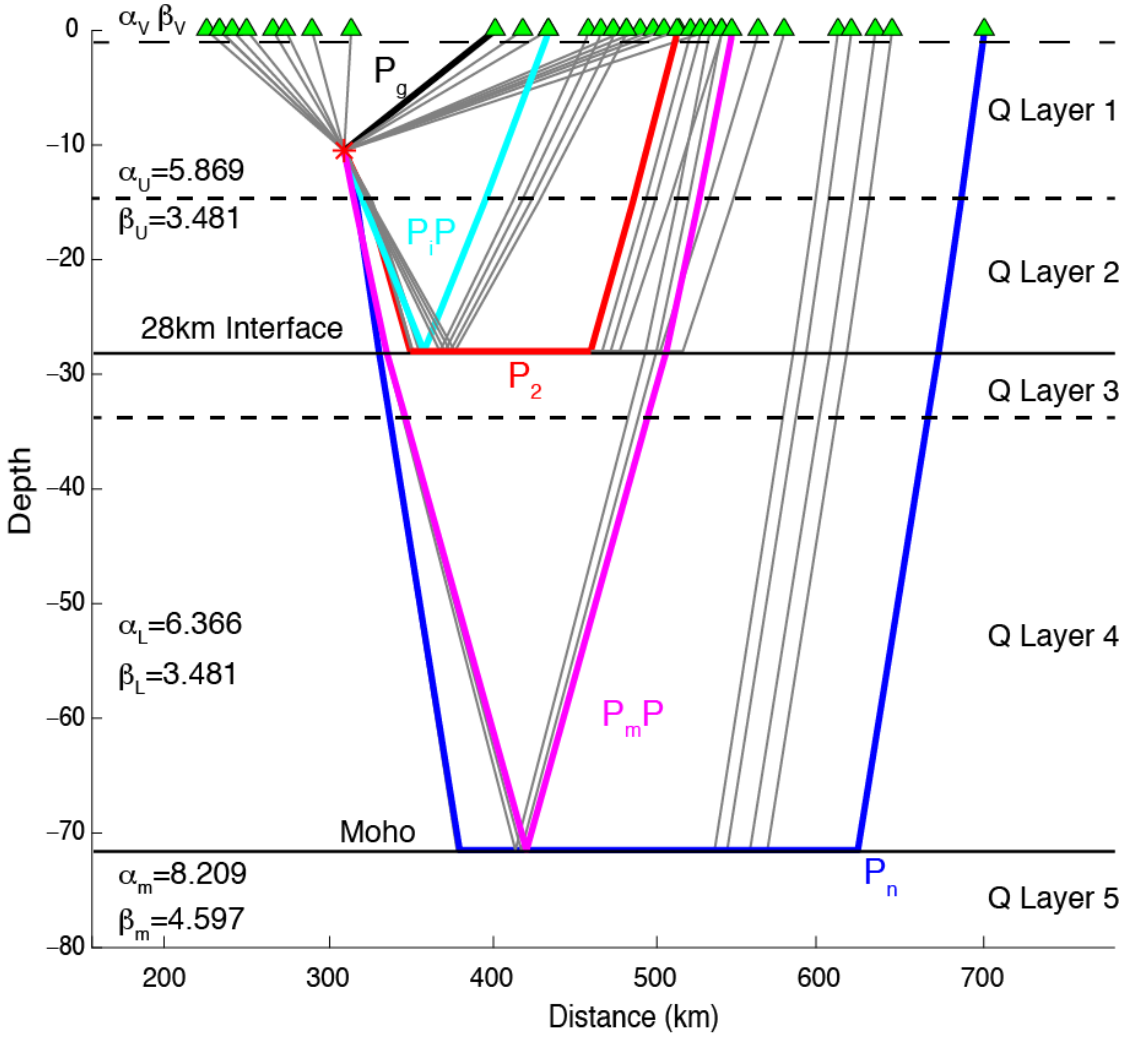
α_V β_V
P_g
Q Layer 1
α_U=5.869
β_U=3.481
P_iP
Q Layer 2
28km Interface
P_2
Q Layer 3
Depth
α_L=6.366
β_L=3.481
Q Layer 4
P_mP
Moho
P_n
α_m=8.209
β_m=4.597
Q Layer 5
0
−10
−20
−30
−40
−50
−60
−70
−80
200
300
400
500
600
700
Distance (km)

Figure 6

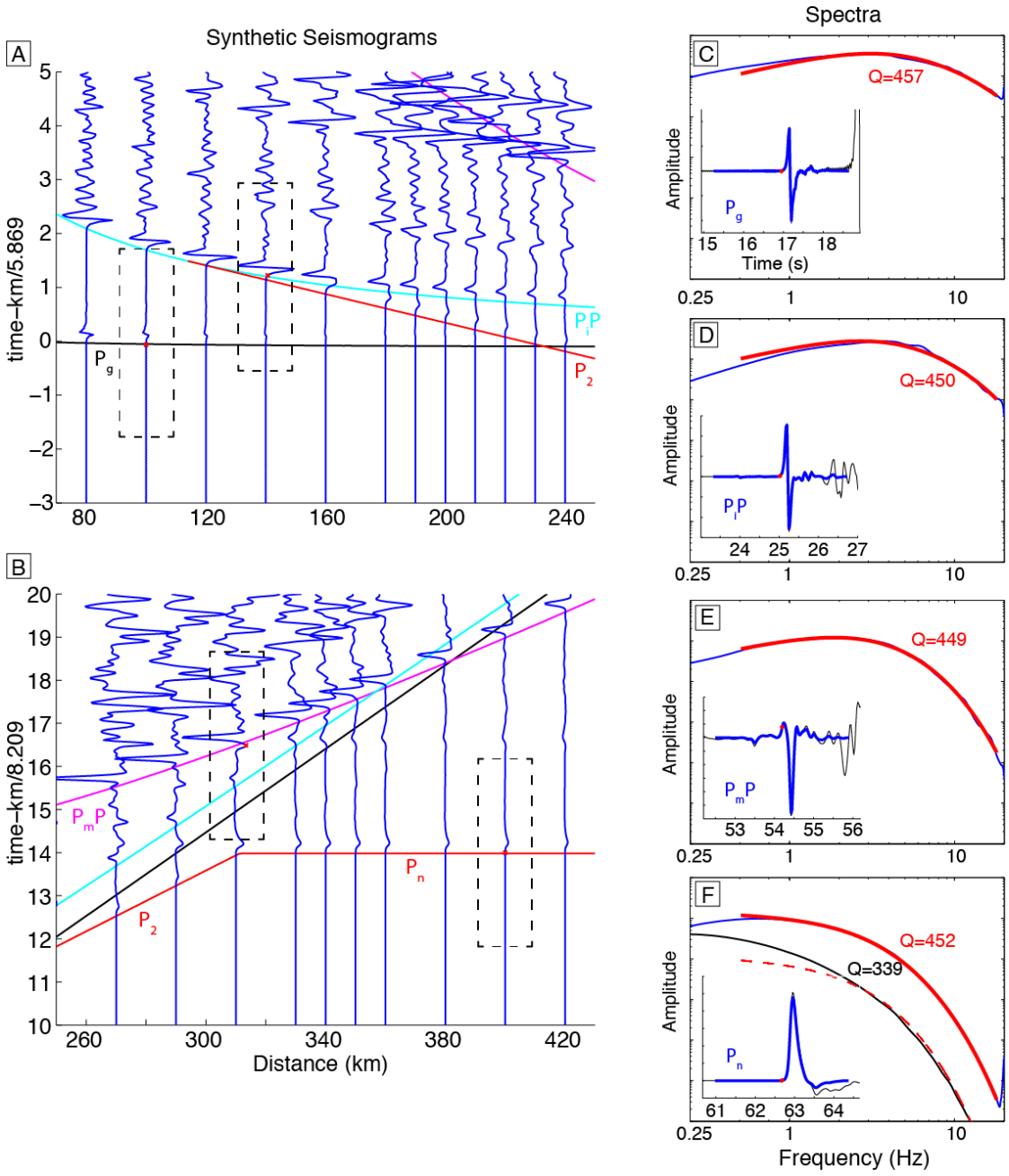
Synthetic Seismograms
A
time−km/5.869
P_g
P_iP
P_2
B
time−km/8.209
P_mP
P_2
P_n
Distance (km)
Spectra
C
Q=457
Amplitude
P_g
Time (s)
D
Q=450
P_iP
E
Q=449
P_mP
F
Q=452
Q=339
P_n
Frequency (Hz)

Figure 7

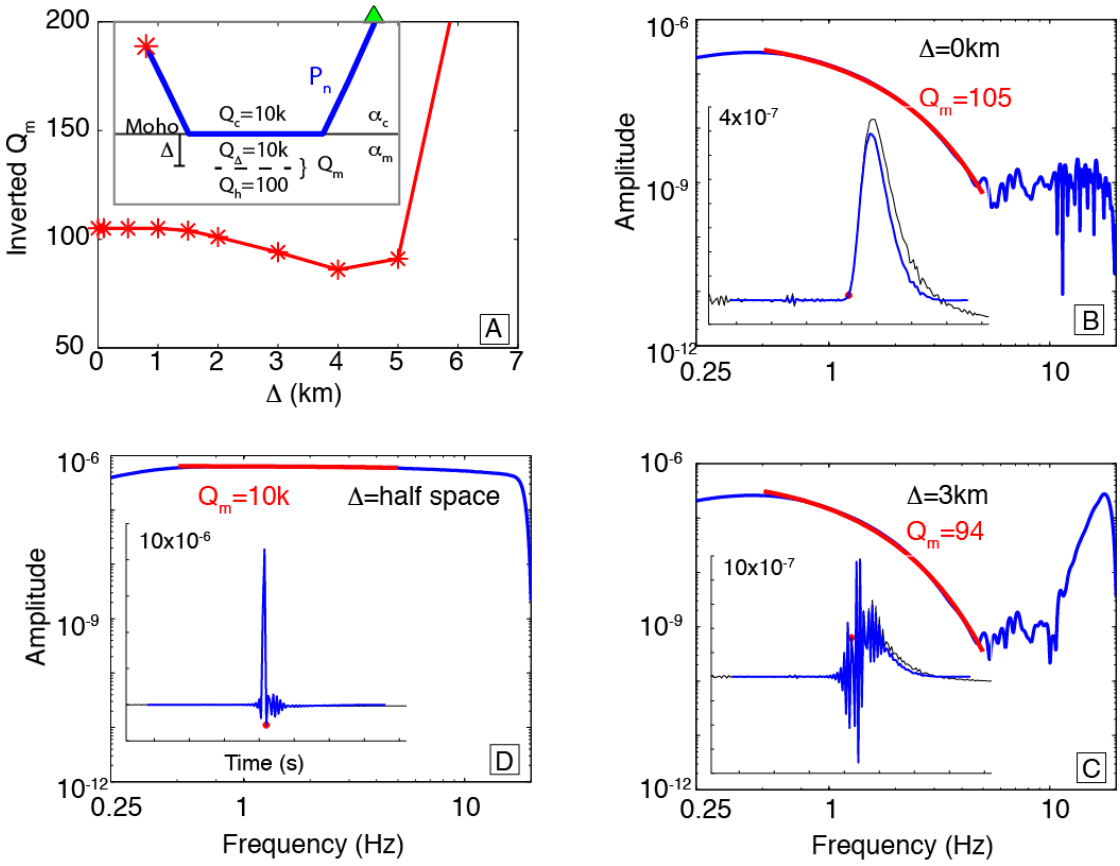
Inverted Q_m
200
150
100
50
0 1 2 3 4 5 6 7
Δ (km)
A
Moho
Δ
P_n
Q_c=10k
α_c
Q_Δ=10k
α_m
Q_h=100
Q_m
Amplitude
10^{-6}
10^{-9}
10^{-12}
0.25 1 10
Frequency (Hz)
Δ=0km
Q_m=105
$4x10^{-7}$
B
Q_m=10k
Δ=half space
$10x10^{-6}$
Time (s)
D
Δ=3km
Q_m=94
$10x10^{-7}$
C

Figure 8

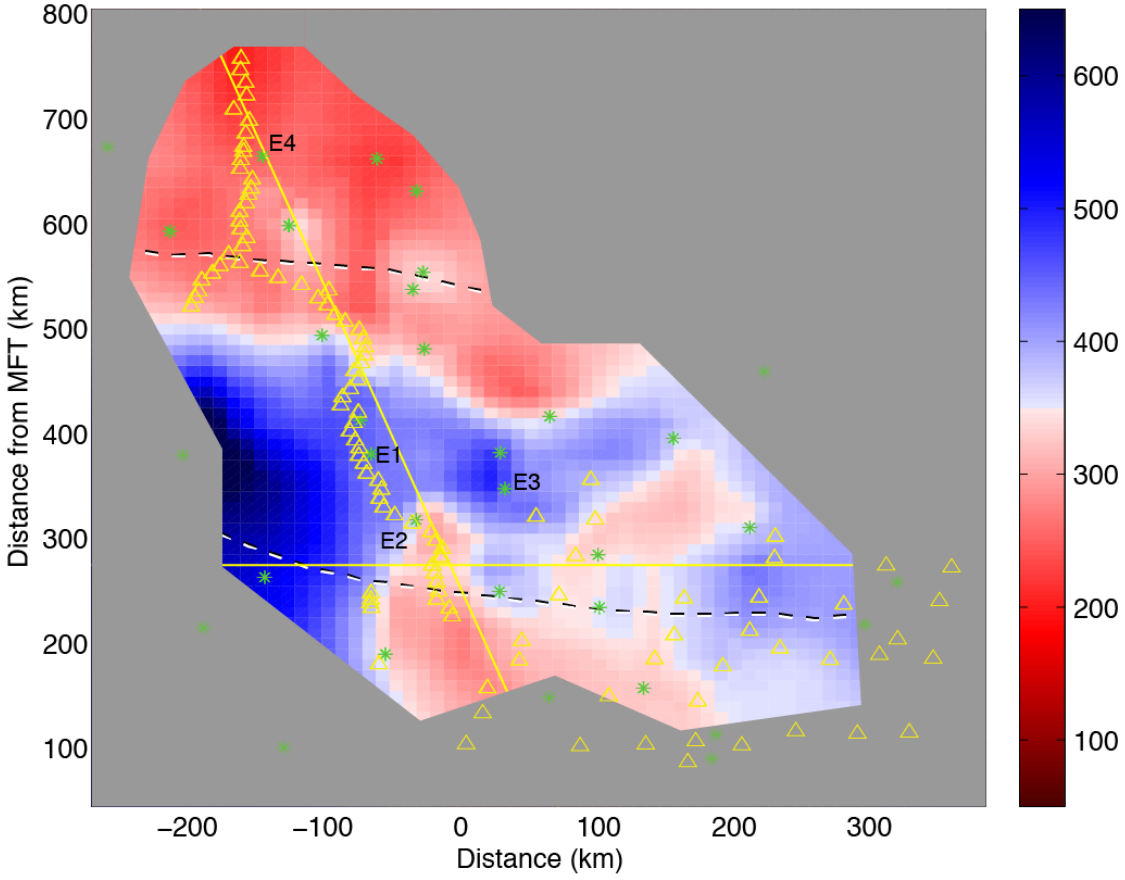
800
700
600
500
400
300
200
100
Distance from MFT (km)
E4
E1
E3
E2
−200
−100
0
100
200
300
Distance (km)
600
500
400
300
200
100

Figure 9

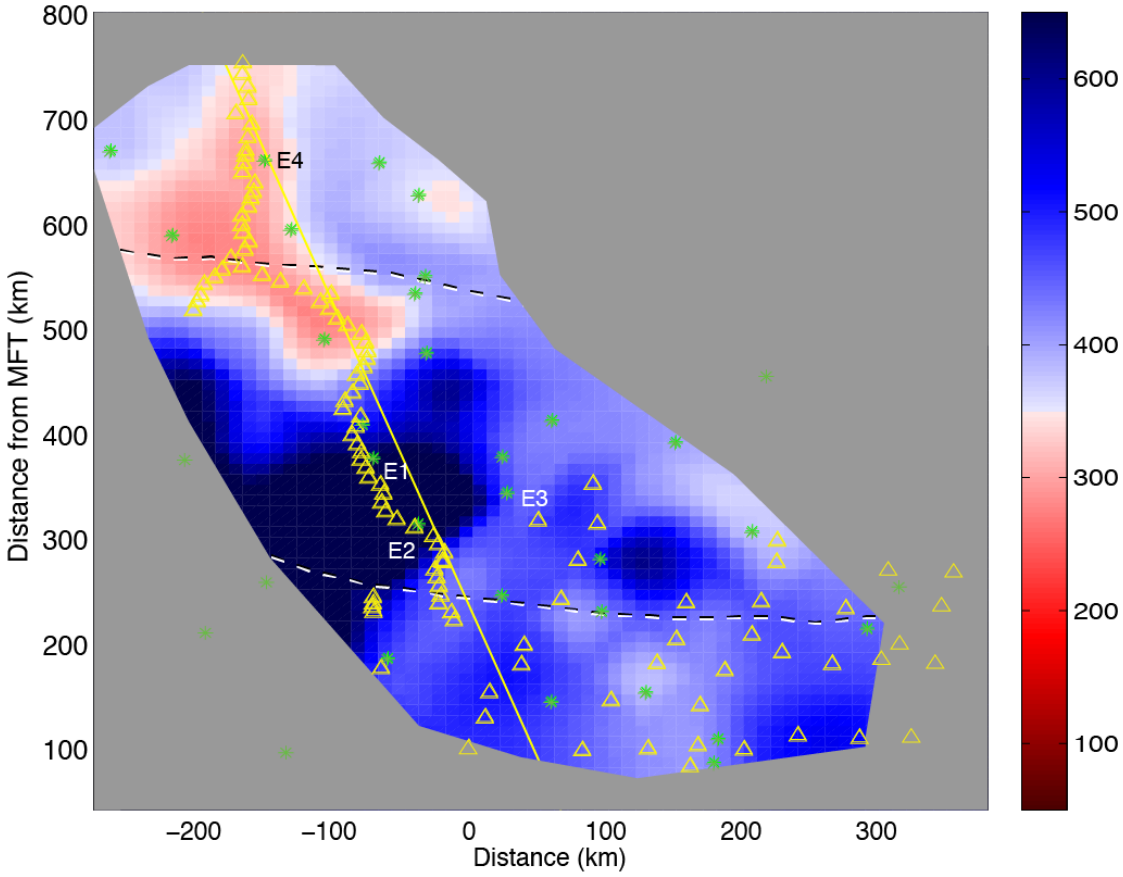
800
700
600
500
400
300
200
100
Distance from MFT (km)
E4
E1
E2
E3
−200
−100
0
100
200
300
Distance (km)
600
500
400
300
200
100

Figure 10

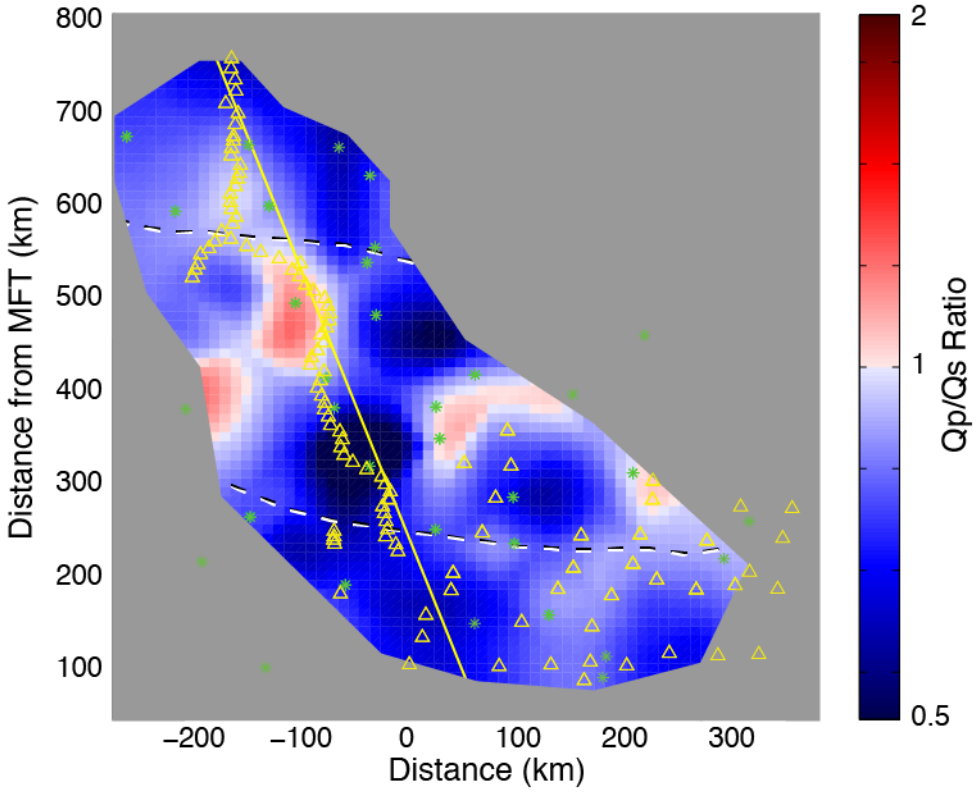
800
700
600
500
400
300
200
100
Distance from MFT (km)
−200
−100
0
100
200
300
Distance (km)
2
1
0.5
Qp/Qs Ratio

Figure 11

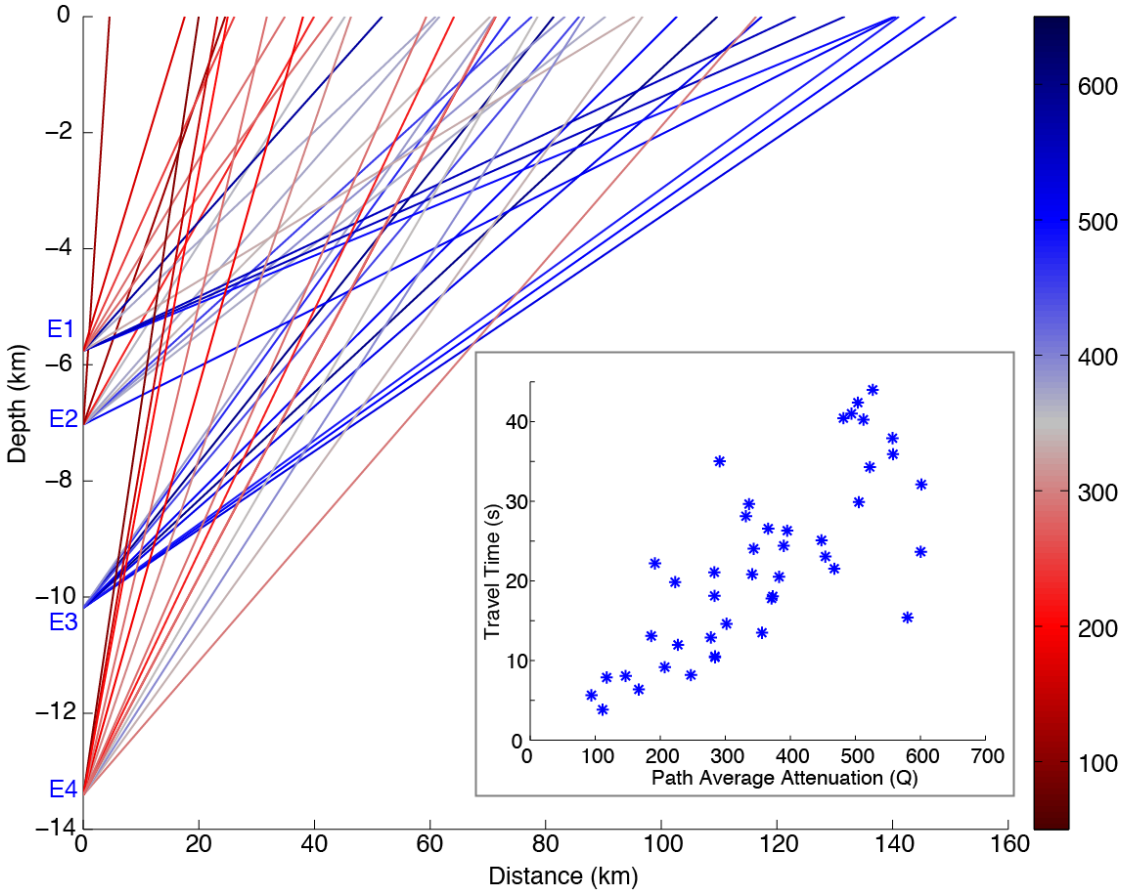
Depth (km)
Distance (km)
E1
E2
E3
E4
Travel Time (s)
Path Average Attenuation (Q)

Figure 12

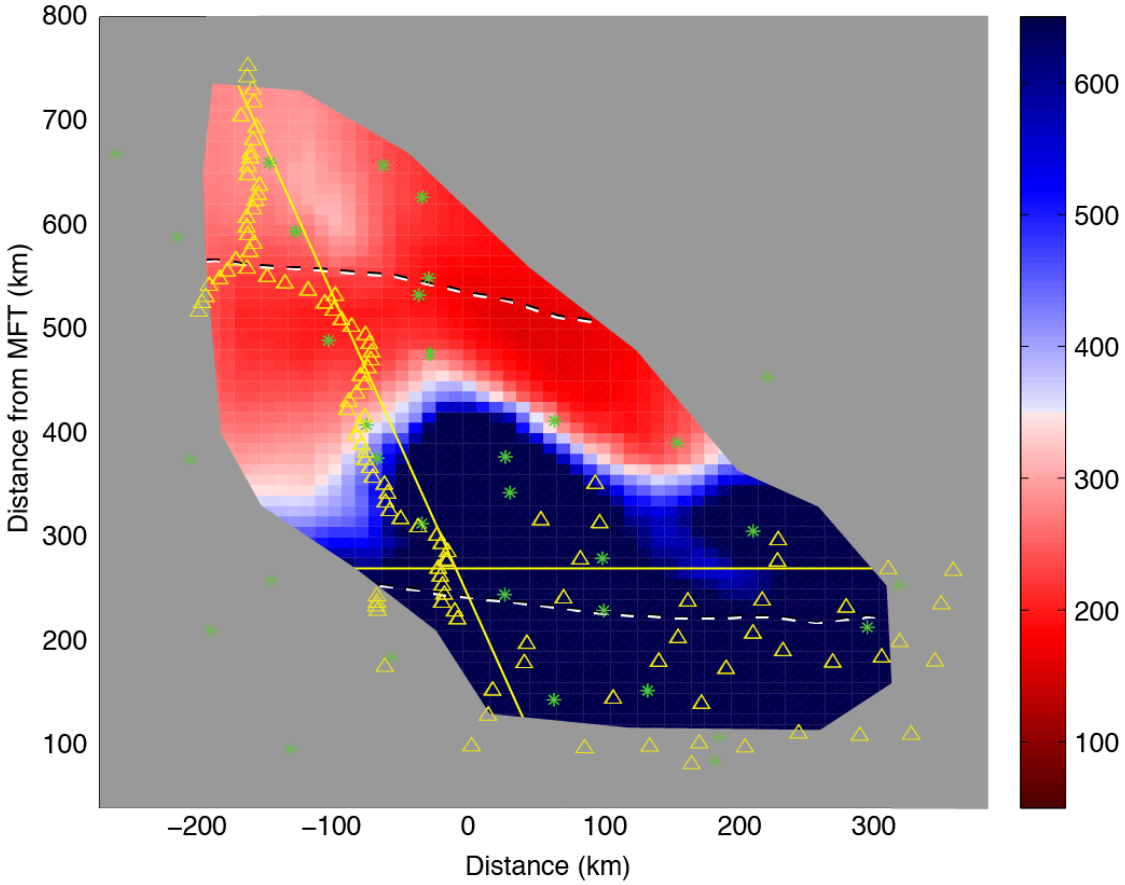
800
700
600
500
400
300
200
100
Distance from MFT (km)
−200
−100
0
100
200
300
Distance (km)
600
500
400
300
200
100

Figure 13

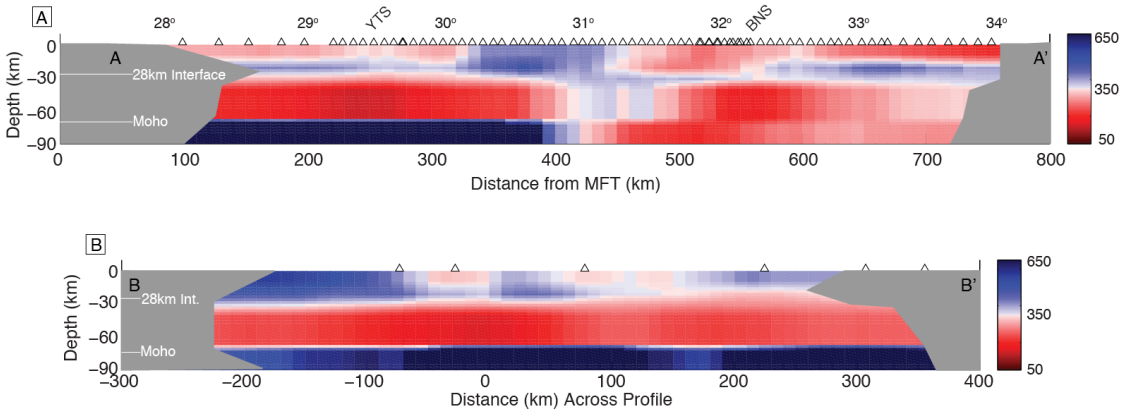
A
28°
29°
YTS
30°
31°
32°
BNS
33°
34°
0
−30
−60
−90
Depth (km)
A
28km Interface
Moho
A'
650
350
50
0
100
200
300
400
500
600
700
800
Distance from MFT (km)
B
0
−30
−60
−90
Depth (km)
B
28km Int.
Moho
B'
650
350
50
−300
−200
−100
0
100
200
300
400
Distance (km) Across Profile

Figure 14

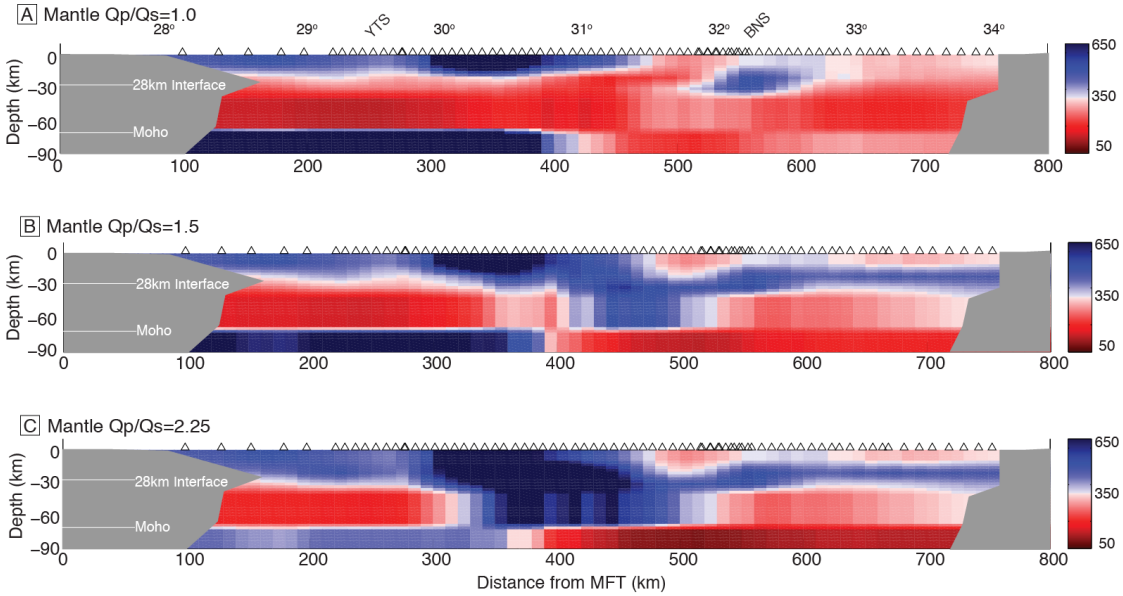
A Mantle Qp/Qs=1.0
B Mantle Qp/Qs=1.5
C Mantle Qp/Qs=2.25
28°
29°
YTS
30°
31°
32°
ENS
33°
34°
28km Interface
Moho
Depth (km)
0
−30
−60
−90
0
100
200
300
400
500
600
700
800
650
350
50
Distance from MFT (km)

Figure 15

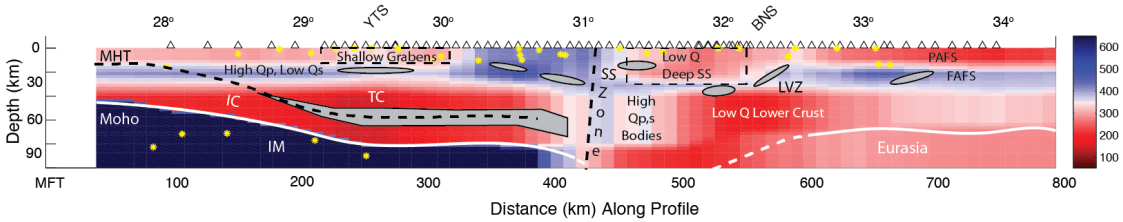
28°
29°
YTS
30°
31°
32°
BNS
33°
34°
0
30
60
90
Depth (km)
MHT
High Qp, Low Qs
Shallow Grabens
IC
TC
Moho
IM
SS
Z
o
n
e
High
Qp,s
Bodies
Low Q
Deep SS
LVZ
Low Q Lower Crust
Eurasia
PAFS
FAFS
600
500
400
300
200
100
MFT
100
200
300
400
500
600
700
800
Distance (km) Along Profile

Table 1

Depth (km)	Qp (± 1σ)	Qs
0-15	338±13	496±30
15-28	325±41	
28-33	377±62	
33-Moho	250±17	
Moho +	409±29	

APPENDICES

A1.0 Figures and Tables Supplemental to Chapter 1

Figures S1-S3. Resolution tests for upper crust *P* and *S*-waves (0-15 km), and upper mantle *P*-waves, respectively. Checkerboard tests were performed using forward modeled data based on ray paths of t^* and SPMS data. Low-resolution regions are shaded opaque gray. Checkers are 50x50 km for upper crust Q_p (Fig. S1), and 100x100 km for upper crust Q_s (Fig. S2) and upper mantle Q_p (Fig. S3) and alternate between Q=250 and 450. Color axis, stations, profiles, and sutures are the same as Figure 8.

Figure S4. Resolution tests for *P* and *S* wave profiles shown in Figures 13 and 14. Color scheme and labels are the same as Figure 13. Data were generated and tested as in Figures S1-S3. **A)** Q_p profile A-A'. **B)** Q_p profile B-B'. **C)** Q_s profile A-A'. Note that A and C profiles cross checkers on a diagonal and therefore a more complex pattern is expected. Also note that Q_s resolution test in C) accounts for Q_p/Q_s ratio so that 15 km-Moho appears as a single layer.

Table S1. Events used in attenuation modeling. Table contains three sections: Upper section contains all events analyzed using SPMS technique. Bold events were the well-resolved reference event and are listed in chronological order. Events listed as

SMPS* were additionally analyzed using *t** method to expand coverage. Middle and lower sections list shallow and deep events, respectively, that were only analyzed using *t** method. Arrivals are the number of catalog first arriving *P* and *S*-phases for each event and do not include reflected arrivals. All deep events are sub- Monigle et al. [2012] Moho (71.5km) and all seismic waveform data from these events are consistent with upper mantle earthquakes.

Figure S1-1

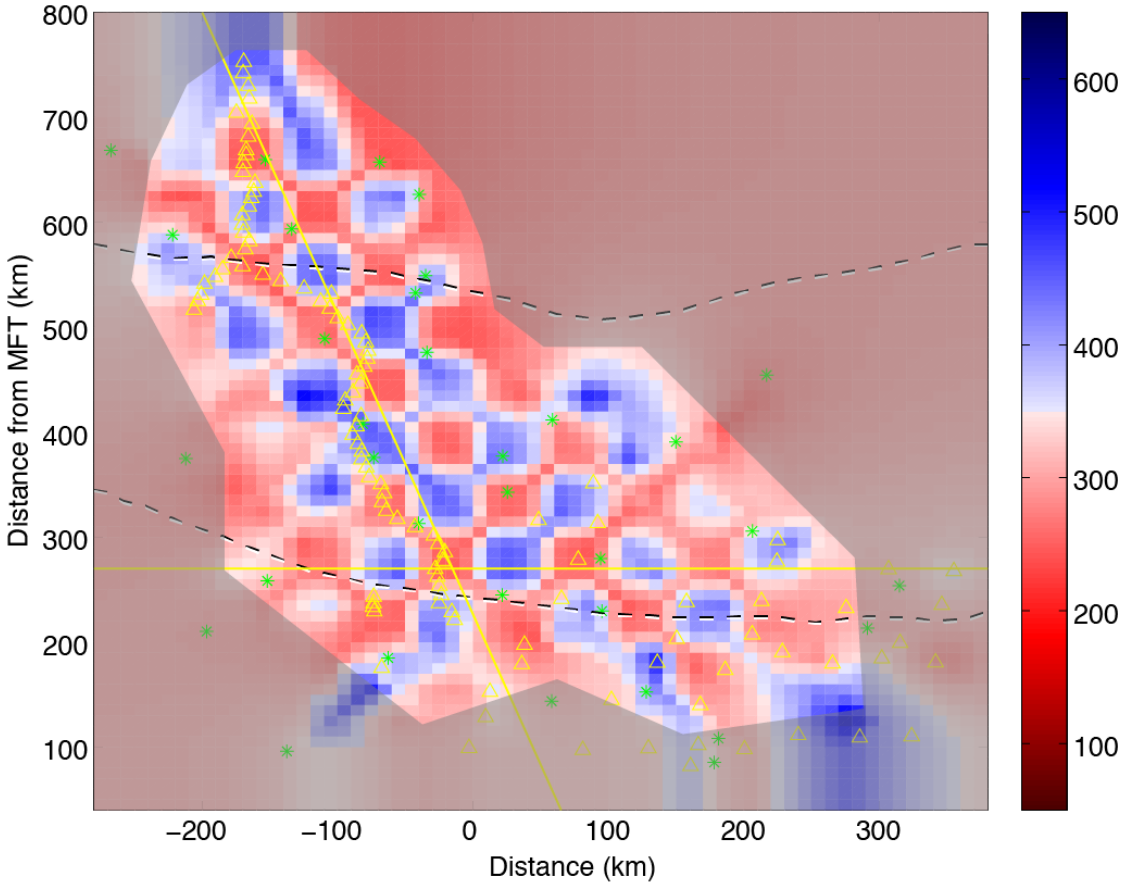
800
700
600
500
400
300
200
100
Distance from MFT (km)
−200
−100
0
100
200
300
Distance (km)
600
500
400
300
200
100

Figure S1-2

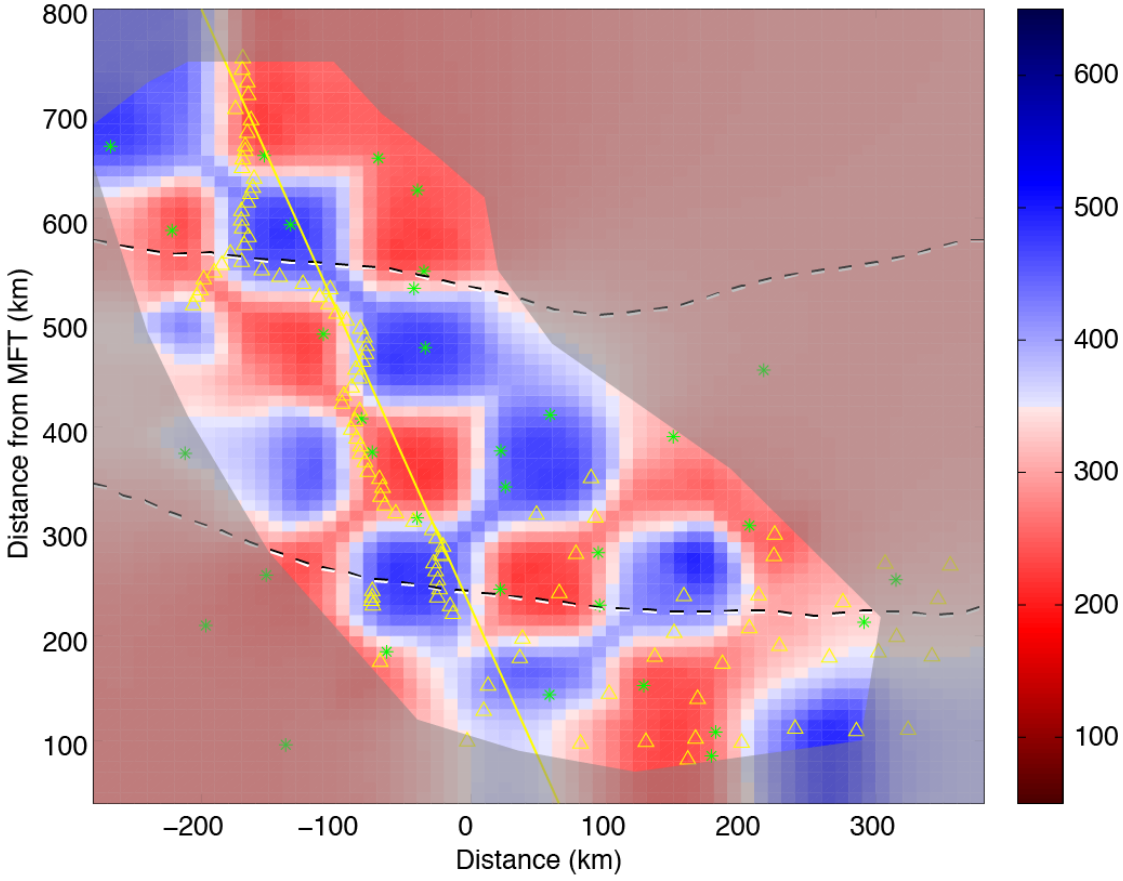
800
700
600
500
400
300
200
100
Distance from MFT (km)
−200
−100
0
100
200
300
Distance (km)
600
500
400
300
200
100

Figure S1-3

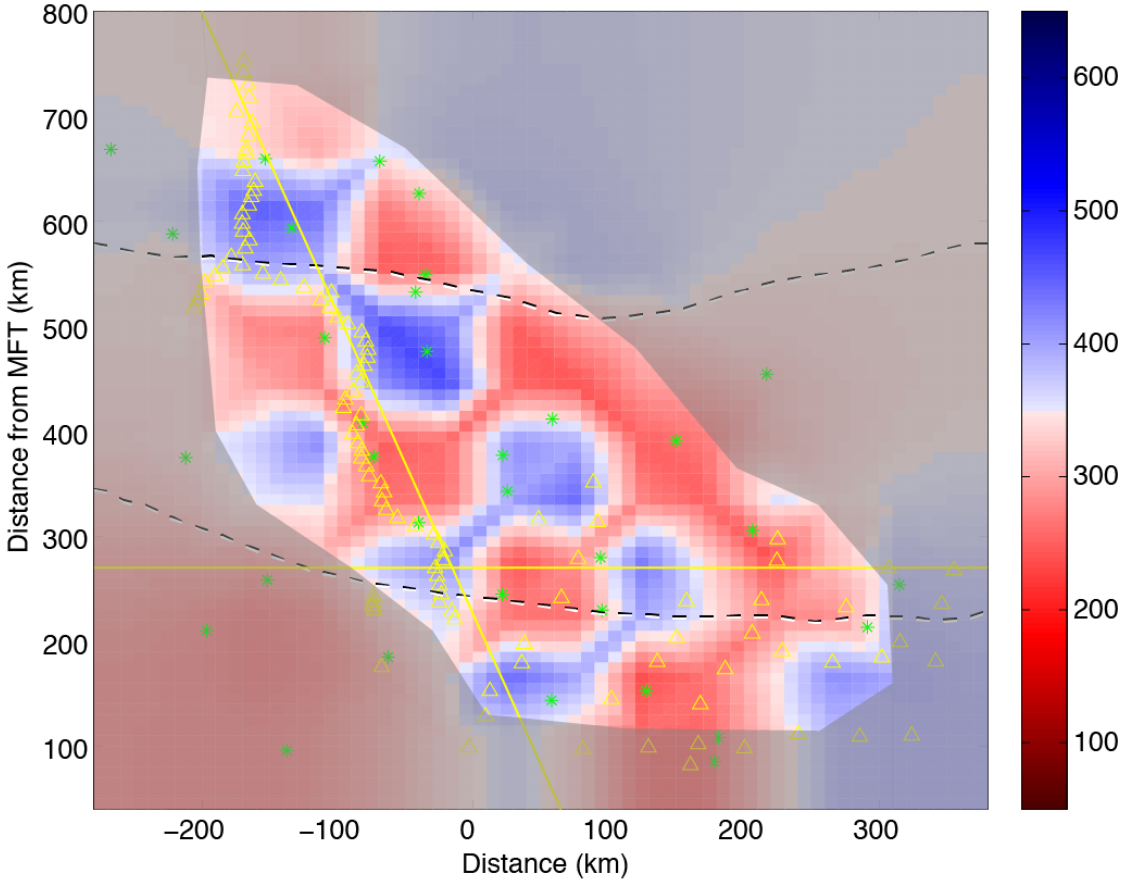
800
700
600
500
400
300
200
100
Distance from MFT (km)
−200
−100
0
100
200
300
Distance (km)
600
500
400
300
200
100

Figure S1-4

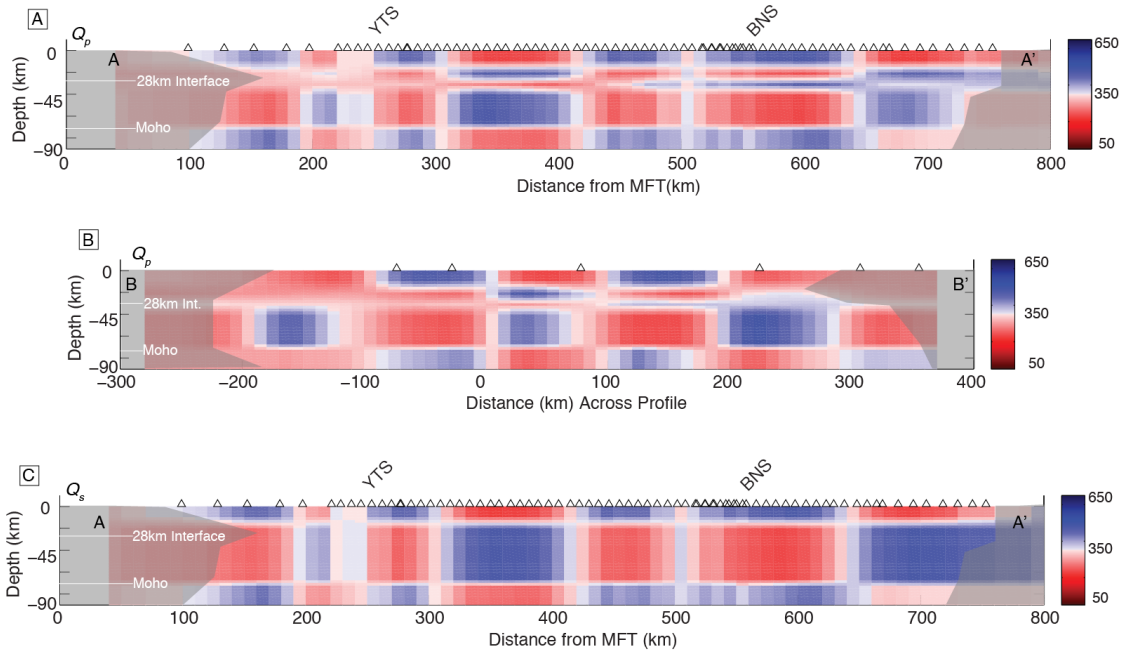
A
Q_p
YTS
BNS
A
A'
28km Interface
Moho
Depth (km)
0
−45
−90
0
100
200
300
400
500
600
700
800
Distance from MFT(km)
650
350
50
B
Q_p
B
B'
28km Int.
Moho
Depth (km)
−300
−200
−100
0
100
200
300
400
Distance (km) Across Profile
C
Q_s
YTS
BNS
A
A'
28km Interface
Moho
Depth (km)
Distance from MFT (km)

Table S1-1

Event Date (DD/MM/YYYY)	Event Time (HH:MM:SS)	Latitude (°N)	Longitude (°E)	Depth (km)	M_L	F_c	Arrivals (#)	Analysis Method
7/8/2004	**21:49:56**	**30.032**	**88.161**	**10.8**	**4.60**	**2.00**	**124**	**SPMS**
7/8/2004	11:29:35	30.034	88.154	10.8	3.80		119	SPMS
8/25/2004	**18:50:41**	**30.366**	**86.266**	**10.2**	**3.84**	**4.50**	**103**	**SPMS**
12/31/2004	18:55:13	30.369	86.258	0.8	3.68		100	SPMS
9/4/2004	**17:36:54**	**30.100**	**85.580**	**7.0**	**3.18**	**4.50**	**110**	**SPMS**
9/15/2004	4:36:27	30.092	85.581	10.5	3.05		101	SPMS
9/20/2004	**6:34:01**	**32.579**	**83.678**	**6.9**	**4.38**	**1.75**	**78**	**SPMS**
9/20/2004	13:45:42	32.577	83.731	3.5	3.62		65	SPMS
10/5/2004	**7:32:29**	**31.686**	**84.854**	**3.5**	**3.56**	**4.75**	**104**	**SPMS***
9/30/2004	13:06:55	31.661	84.801	2.2	3.09		86	SPMS
11/5/2004	**22:15:15**	**30.987**	**86.614**	**5.7**	**4.01**	**4.75**	**87**	**SPMS**
11/4/2004	2:54:40	30.978	86.603	0.8	3.77		83	SPMS
12/4/2004	**13:07:56**	**32.079**	**85.556**	**0.0**	**3.02**	**4.75**	**99**	**SPMS**
12/28/2004	20:08:41	32.036	85.541	4.1	3.28		85	SPMS
12/8/2004	**22:48:37**	**29.796**	**86.987**	**0.3**	**3.00**	**3.25**	**126**	**SPMS***
12/8/2004	22:57:20	29.799	86.984	3.9	2.42		95	SPMS
12/19/2004	**2:36:27**	**29.169**	**83.940**	**4.1**	**3.18**	**4.75**	**97**	**SPMS**
1/27/2005	22:14:39	29.143	83.923	2.6	3.21		82	SPMS
1/29/2005	**0:50:45**	**33.203**	**85.279**	**0.0**	**3.07**	**5.50**	**55**	**SPMS**
2/3/2005	21:25:39	33.202	85.251	0.0	3.12		57	SPMS
3/25/2005	**15:59:08**	**31.374**	**88.271**	**0.0**	**4.03**	**2.50**	**67**	**SPMS***
8/20/2005	12:50:44	31.305	88.201	6.0	5.09		80	SPMS
5/11/2005	**4:13:00**	**30.665**	**85.232**	**5.8**	**4.67**	**1.50**	**148**	**SPMS**
5/11/2005	0:45:36	30.672	85.235	8.7	2.83		112	SPMS
7/3/2005	**22:09:35**	**31.569**	**85.644**	**4.1**	**3.34**	**3.75**	**91**	**SPMS**
7/4/2005	10:27:59	31.576	85.647	6.6	3.29		90	SPMS
6/22/2004	7:07:21	28.942	85.344	0.8	3.02	6.50	59	t*
7/9/2004	7:38:13	33.306	83.200	13.9	4.01	2.00	61	t*
8/14/2004	5:37:03	30.800	87.569	1.6	3.32	2.50	84	t*
8/24/2004	11:37:28	32.227	85.634	0.0	3.13	3.00	82	t*
10/30/2004	11:12:51	30.656	83.780	0.5	4.06	2.00	106	t*
11/17/2004	10:38:58	28.139	84.561	15.7	3.86	4.50	83	t*
1/13/2005	4:53:39	29.482	86.225	0.4	3.19	10.00	74	t*
1/16/2005	20:58:36	32.629	84.598	0.0	3.36	3.75	72	t*
1/25/2005	20:52:16	32.927	85.584	0.0	3.35	3.25	70	t*
2/16/2005	2:33:56	30.953	85.150	5.1	2.59	6.25	91	t*
4/6/2005	22:24:36	30.676	86.230	9.8	4.12	2.75	101	t*
5/10/2005	21:47:53	28.649	87.339	4.7	2.51	6.25	63	t*
5/26/2005	11:30:36	29.344	86.998	0.7	3.20	4.00	56	t*
6/11/2005	12:59:21	33.225	84.394	13.4	3.01	5.75	59	t*
7/12/2005	8:08:46	29.604	84.410	0.0	3.38	3.00	67	t*
10/10/2004	11:48:47	28.043	87.865	82.6	3.72	2.00	84	t*
11/6/2004	4:33:27	29.568	89.312	91.4	3.63	3.50	70	t*
12/1/2004	3:25:23	28.566	86.601	78.1	3.59	7.50	82	t*
12/8/04	13:02:47	29.199	89.050	76.9	3.26	4.50	89	t*
3/26/2005	20:32:13	28.250	87.898	71.6	5.10	1.75	77	t*

Evidence for low-angle normal faulting in the Pumqu-Xianza Rift, Tibet

Patrick W. Monigle[1], John L. Nabelek[1], Jochen Braunmiller[1,2], N. Seth Carpenter[1,3]*

[1]Oregon State University, College of Earth, Ocean, and Atmospheric Sciences, Corvallis, Oregon, USA

[2]Now with University of South Florida, College of Arts and Sciences, Tampa, Florida, USA

[3]Now with Kentucky Geological Survey, Lexington, KY, USA

*Corresponding author e-mail: pmonigle@coas.oregonstate.edu

Accepted to Geophysical Journal International 15 June, 2012

The Royal Astronomical Society

Great Clarendon St., Oxford, UK

A2.0 Evidence for low-angle normal faulting in the Pumqu Xianza Rift, Tibet

A2.1 Summary

Low-angle normal faulting is widely discussed as a possible mechanism for continental extension, however, unambiguous evidence for seismogenic low-angle normal faulting is lacking. Here we investigate seismicity along a short segment of the Pumqu-Xianza Rift (PXR) in southern Tibet, where the HiCLIMB seismic array recorded over 500 earthquakes between July 2004 and August 2005. Hypocenters of the 40 best-recorded earthquakes are approximately 20-25 km west of the rift and tightly clustered at about 10 km depth, consistent with moment tensor depths of the 11 largest ($3.4 \leq M_w \leq 4.5$) earthquakes. Events in this group have N-S striking normal faulting mechanisms with low-angle (29°) west-dipping fault planes. Rupture along a west-dipping, low-angle, planar normal fault (the eastern PXR boundary fault) is consistent with event hypocenters, fault dip from moment tensors, and prominent surface morphology. The dip of 29° is at the low end of physically possible values assuming normal frictional behavior and state of stress. We suggest it is possible for a planar, low-angle fault to nucleate seismically at a low-angle at depth in the presence of basal shear and work its way aseismically through the brittle crust to the surface with the aid of lubricating minerals.

A2.2 Introduction

Under Andersonian stress distribution (Anderson, 1951) and Coulomb rock strength conditions, brittle normal faults should initiate with dips of about 60°. For previously faulted rocks, following Byerlee's (1978) friction law, the range of possible normal-fault dips is substantially larger. A limiting frictional lock-up is expected to occur at about 30° dip (Sibson, 1985). Global compilations of focal mechanisms of normal-faulting earthquakes with unambiguously identified fault planes show dip angles between 40°-60° and only a few documented cases exist in the 30°-40° range (Jackson & White, 1989; Abers et al., 1997; Doser, 1987; Collettini & Sibson, 2001). However, low-angle normal faults with dips smaller than 30° have been observed in surface geology and in seismic reflection profiles at shallow depths in the upper crust (e.g., Wernicke, 1995; Lister & Davis, 1989). It has been suggested these faults have been rotated from an initial steeper angle by flexure due to isostatic response (Buck, 1988; Spencer & Chase, 1989) or they are the result of departures from Andersonian stress distribution at depth (Melosh, 1990; Westaway, 1999).

Shallow seismicity in the Lhasa Block in southern Tibet occurs primarily along N-S trending grabens. Elliott et al. (2010) analyzed teleseismic body-wave and InSAR data from larger ($M_w \geq 5.9$) normal-faulting earthquakes to address their fault geometry and found fault planes with 40° to 50° dips. Here we investigate vigorous seismicity associated with the Pumqu-Xianza Rift (PXR) (earlier noted by Langin et al., 2003) recorded by the HiCLIMB seismic array between July 2004 and August 2005, when the station distribution provides azimuthal coverage for accurate hypocenter

determination (Fig. S2-1) (Nabelek et al., 2009). During these 14 months, over 500 well-located events occurred in the PXR region (Fig. S2-1) (Carpenter et al., 2010).

The PXR extends south from the Gyaring Co transform fault, across the Yarlung-Tsangpo Suture (YTS), to the Pumqu River, which it follows to the Himalayan range (Armijo et al., 1986). High seismicity during HiCLIMB occurred along a 16-km well-formed section of the PXR near the village of Qingdu (Fig. S2-1). Recent PXR earthquake activity (ISC $m_b \geq 4.0$) began in 1980 with an M_w 6.4 event near the northern end of the graben, followed by aftershocks and sporadic activity through the mid 1980's. Seismicity returned in 1994, with activity clustered south of the 1980's events including M_w 5.7 and 5.9 events in 1996 and 1998. The Qingdu segment has been active since 1994 and the last two reported earthquakes occurred in 2010. We use HiCLIMB data to relocate the 50 best-recorded earthquakes ($2.1 \leq M_L \leq 5.0$) and to determine 12 regional moment tensors (RMT). Our results provide evidence for active, low-angle (29°) normal faulting.

A2.3 Data Analysis

Earthquakes were selected from the catalog of Carpenter et al. (2010) (Fig. S2-1), which is based on automatic phase picks from the HiCLIMB phase-2 deployment (Fig. S2-1 inset). The catalog lists over 500 well-located earthquakes (with at least 20 P- and S-arrivals) in the study area. Forty earthquakes with more than 35 P- and S-arrivals were selected from the cluster west of Qingdu and ten additional events based

on their proximity to stations south of Qingdu. P- and S-arrivals for each event were inspected and adjusted manually; numerous P- and S-arrivals were added. On average, manually located events show only a small southwestward shift of 2.2 km (standard deviation: 1.8 km) from the Carpenter et al. (2010) catalog.

Earthquake hypocenters (Fig. S2-2; Table S2-1) were determined by least-squares travel-time inversion using GENLOC (Pavlis et al., 2004). Uniform P- and S-wave arrival uncertainties were assigned based on overall pick uncertainty (0.2 and 0.5 s, respectively) and distance weighting was implemented with full weighting of arrivals to 2° distance, reducing linearly to zero weight beyond 3° distance. We used two crust/upper mantle velocity models (Fig. S2-5): a receiver function model for this region (Nabelek et al., 2009) and a travel-time-based model calculated from P_g, P_n, S_g, and S_n arrivals identified in this study. Hypocenter locations were similar for both models. Tests using different starting depths produced essentially identical results. The mean horizontal error ellipse (1-σ) has a major axis of 1.7 km (max. 3.0 km) and minor axis of 0.8 km, striking 40°; the depth error is 0.5 km (max. 1.1 km). The combination of P- and S-arrivals from the closest stations and P_n phases control the estimated depth. The maximum station azimuthal gap is 155° (no coverage at azimuths 300° to 95°) for events west of Qingdu and less than 90° for events south of Qingdu.

In all, 40 events were located in a cluster 20-25 km west from the east-wall fault scarp of the PXR (Fig. S2-2). These events range from 6-12 km depth, with a lateral spread of 5 km east-west and 6 km north-south. Double-difference relative

locations (Waldhauser & Ellsworth, 2000) exhibit a similar tight cluster. We found no discernible temporal event migration pattern. Another seven events, at 6-9 km depth, were located within the PXR valley near station T0370 and three small events ($2.2 \leq M_L \leq 2.5$) occurred further south near T0320.

Regional moment tensor (RMT) solutions were determined from complete 3-component seismograms (Fig. S2-6 and Table S2-2) following Nabelek & Xia (1995). The receiver function model was reduced to a slowness-balanced, 8-layer model for RMT calculations (Fig. S2-5) and results with the travel-time-based model were essentially identical. Moment tensors were constrained to be deviatoric and data were weighted based on epicenter-station azimuth, with equal weight for each thirty-degree sector.

RMT analysis was performed on 12 earthquakes ($3.2 \leq M_w \leq 4.5$). Eleven events in the cluster west of the graben (Fig. S2-2) were analyzed in the 20-50 s band with, on average, 47 seismograms. They have normal faulting mechanisms with mean nodal planes of 179°/29°/–82° and 351°/61°/–94° (strike/dip/rake). Dip is the best-resolved parameter and for the best-constrained events dip uncertainty, based on conservative 5% variance increase, is between 3° and 4°. Analysis in the 10-30 s band on these 11 events gave similar results, with a slight decrease in dip for the west-dipping nodal planes (mean: 180°/23°/–88°). The smallest event occurred inside the graben near T0370 and could only be analyzed in the 10-30 s band. This event has a strike-slip mechanism.

A2.4 Discussion

The northern PXR is variably expressed (Fig. S2-1 and S2-2). At its north end, near Xianza, the western wall is a prominent fault scarp, while to the east no clear valley-bounding fault exists. As the PXR approaches the Qingdu segment from the north, the eastern wall becomes a sharp bounding fault, while the western boundary becomes structurally subdued. At about 30.1°N, the PXR steps west into the Qingdu segment, which is a 16-km long and 8-10 km wide half-graben with an apparent bounding fault on the eastern side of the valley. Immediately south of Qingdu and T0370, the eastern wall of the Qingdu valley terminates; its continuation becomes a prominent fault of an east-dipping half-graben.

Seismicity since 1994 (Fig. S2-1) is focused on the Qingdu region (29.7°-30.3°N), but well west of the valley and with diffuse activity continuing north and south of the actual Qingdu segment. During the HiCLIMB deployment, seismicity was high, tightly clustered 20-25 km west of the east-bounding wall of the PXR and focused on the Qingdu segment (Fig. S2-2). Relocation places the six earthquakes listed in the ISC catalog into this tight cluster, suggesting the full spread of ISC events (as shown in Fig. S2-1) may not be accurate, though their overall westward shift relative to the PXR is probably real.

Based on our relocations and the Carpenter et al. (2010) catalog, the entire Qingdu segment was seismically active during the HiCLIMB deployment (Fig. S2-2). The north-south extent of seismicity appears to be bound by the Qingdu segment

boundaries. The events are west of the rift and have normal faulting mechanisms with N-S striking nodal planes. Hypocenters are at 9-12 km depths from location and moment tensor analysis. Nodal plane dips, well resolved from waveform modeling (Fig. S2-6), indicate rupture either on a shallow 29° westward-dipping fault or on a 61° steeply eastward-dipping fault.

In addition to high seismicity west of the rift, several small ($M_w \leq 3.2$) earthquakes occurred directly under the half-graben just south of T0370 (Fig. S2-2). The single RMT solution established for these events is strike-slip, suggesting they could represent E-W transform motion between the footwalls of west- and east-dipping normal faults as the PXR steps east south of Qingdu, consistent with current motion on these main faults.

Fig. S2-3 shows possible faulting interpretations consistent with RMT solutions and hypocenter locations. Our preferred interpretation is that the earthquakes west of the PXR occurred along a planar, west-dipping, low-angle (dip 29°) normal fault surfacing at the eastern boundary wall of the PXR, a prominent fault scarp on satellite imagery. The earthquake hypocenters are just above the top of a low-velocity zone imaged by receiver functions (Nabelek et al., 2009) and near the base of the brittle upper crust. This is the simplest interpretation that geometrically connects seismic observations at depth with surface morphology.

We cannot, however, preclude other interpretations because slip from none of the earthquakes ($M_w \leq 4.5$), with faulting dimensions of about 1 km^2, reached the surface and because the hypocenters do not define a fault plane. The events could have

occurred on a minor fault with no surface expression and not associated with the PXR. A west-dipping listric fault (dash-dotted line in Fig. S2-3) or a steep (61°) east-dipping fault (dotted line in Fig. S2-3), both west of the PXR, cannot be ruled out. Activity along previously unmapped faults or faults without obvious geomorphic surface expression has been documented for several normal faulting earthquakes in Tibet (M_w 5.9-6.4) with high-angle fault plane solutions (40°-50°) by Elliot et al. (2010).

However, the following observations combined support the interpretation that the seismicity described here is related to the west-dipping eastern bounding fault of the Qingdu segment: 1) The earthquakes have hypocenters and moment tensor mechanisms consistent with a planar fault reaching the surface at the eastern side of the Qingdu valley. 2) The eastern fault scarp in the Qingdu valley is a dominant feature indicating Holocene movement. 3) Seismicity correlates with the north-south length of the Qingdu valley. 4) Transform-fault events inside the Qingdu valley indicate active motion on the main PXR normal faults.

Seismogenic normal faulting along crustal-scale faults dipping 40° or less has been documented only in a few cases, with dips near or below 30° being extremely rare (Jackson & White, 1989; Collettini & Sibson, 2001). The most striking examples come from earthquakes within the Woodlark basin (Abers, 1991; Abers et al., 1997) where body wave modeling indicates 24°-35° dips for several events; a 32° dip for a 1970 event near Moresby Seamount is supported by independent seismic reflection data. Shallow fault dips have also been found for earthquakes in the western Gulf of Corinth with 30°±5° for the 1995 Aigion earthquake (Bernard et al., 1997) and 30°±3°

for the 1992 Galaxidi earthquake (Hatzfeld et al., 1996), but not for events in the eastern part of the gulf, which dip near 40° (Braunmiller & Nabelek, 1996). The 1946 Ancash, Peru earthquake is possibly another example for 30° normal faulting (Doser, 1987). Surface ruptures were mapped near, but not on, pre-existing thrust faults dipping 25°-35°, with the main surface scarp from the earthquake dipping at 42° (Doser, 1987). Given the limited waveform data available, dip uncertainty could be larger than the 10° reported. Detachment faults dipping 0°-20° have been observed geologically (Wernicke, 1995), but whether such faults slip seismically is not clear. Eyidogan & Jackson (1985) modeled waveform complexities for events in western Turkey as sub-horizontal detachment faulting, though reanalysis by Braunmiller & Nabelek (1996) shows the events are planar with dips near 40°.

The physical processes driving low-angle faulting are poorly understood. Frictional lock-up, prohibiting further slip on pre-existing faults, is expected to occur at about 30°-40° dip for Andersonian stress distribution and a typical coefficient of friction near 0.6 (Fig. S2-4) (Sibson, 1985; Collettini & Sibson, 2001). Slip on faults shallower than 30° requires stress-field rotation (Melosh, 1990; Westaway, 1999) or fault weakening, possibly through a combination of a lower friction coefficient m and increased pore pressure (Collettini & Sibson, 2001).

The dips for the PXR events, assuming they occurred on the west-dipping fault, range from 22° to 33° (mean value 29°), which, at 22°, would be locked-up. The top of a low-velocity zone (Nabelek et al., 2009) at 15-20 km depth in the Lhasa Block probably defines the base of the seismogenic zone. Shear at this base may rotate the

stress-field (Westaway, 1999) enabling seismic activity along a low-angle normal fault at the base of the brittle crust as observed here. The cause for basal shear could be traction from the sub-horizontal motion of the Indian plate along the Main Himalayan Thrust (MHT) (McCaffrey & Nabelek, 1998), which is at about 45 km depth in the Lhasa Block (Nabelek et al., 2009); this traction requires a well-coupled plate interface and a high-viscosity middle crust above the interface (Copley et al., 2011).

At shallower depths, significant deviations from Andersonian stress distribution are unlikely and to extend seismic slip along a low-angle fault to the surface requires a weak fault. This could be achieved by geothermally-driven increased pore fluid pressure and/or a reduction of friction along the fault zone to μ=0.3-0.4 (Fig. S2-4). High heat flow and abundant geothermal activity are associated with grabens in Tibet (Armijo et al., 1986). Fluid presence would aid chemical weathering leading to deposits of weak phyllosilicates (e.g., clay, talc) in a fault zone. Fault material containing the clay mineral smectite with μ=0.21 was found at 2.7 km depth on the San Andreas Fault in a segment characterized by stable creep (Carpenter et al., 2011). Talc has a friction coefficient of 0.1-0.2 and is stable over a wide temperature range (Moore & Lockner, 2008) and hence it can be potentially present over a wide depth range within a fault zone. Phyllosilicates, however, exhibit velocity strengthening frictional behavior and their presence would result in aseismic creep rather than seismic slip on a fault.

Low-angle (~30°) normal faults have been also identified in the shallow crust in the Lunggar rift (Kapp et al., 2008) and the Yadong-Gulu rift (Cogan et al., 1998) in

the Lhasa Block. So far, it has not been determined how deep the shallow-dipping parts of these faults extend or if they are seismogenic. The Yadong-Gulu rift fault has been interpreted in terms of a rolling-hinge model with a steeper, active part extending into the deeper seismogenic zone (Cogan et al., 1998). The Lunggar rift is described as an evolutionary structure that initiated as a steep fault and subsequently rotated into its present 30° dip (Kapp et al., 2008). We suggest that a planar, 30°-dip fault can be created without rotation from initially steep inclination under special conditions: shear traction at the base of the seismogenic layer and an environment conducive to the generation of phyllosilicates. Initiating at the base of the brittle crust in a seismic fashion, in the presence of a basal traction, low-angle faulting may work its way to the surface by creep enabled through fluid influx progressively lining the developing fault interface with lubricating minerals. For a creeping, lubricated fault we would expect substantially reduced numbers of higher magnitude earthquakes (Amelung & King, 1997).

A2.5 Conclusions

Our study is one of few to support low-angle normal faulting from earthquake source mechanisms. We provide evidence for faulting with dips in the range of 22° to 33° from well-resolved earthquake RMT solutions. Combined with the hypocenter locations, such faulting is consistent with activity on the west-dipping eastern PXR fault, which shows prominent surface morphology. The dips are at the low end of or

below physically possible values assuming normal frictional behavior (Collettini & Sibson, 2001). The earthquakes occurred near the base of the seismogenic layer (Nabelek et al., 2009). Traction at the base of the seismogenic layer transmitted upwards from the MHT (McCaffrey & Nabelek, 1998; Copley et al., 2011) may rotate the stress field to enable brittle, low-angle normal slip. To extend slip along a low-angle normal fault to the surface requires a decrease in effective fault friction (strength), which may be achieved by lining the fault with phyllosilicates and/or by increasing the fluid pressure in the fault zone. The presence of phyllosilicates, though, would probably render slip in the upper fault zone aseismic, at least for crustal-scale earthquakes. Our results from PXR indicate that 30° planar faults can form and extend across the entire brittle crust in the Lhasa Block.

A2.6 Acknowledgements

This study was supported by the NSF, Continental Dynamics Program, grant EAR 9909609 and the Air Force Research Laboratory, contract FA8718-09-C-0004. The authors wish to thank C. Collettini and two anonymous reviewers for comments.

A2.7 References

Abers, G.A. 1991, Possible seismogenic shallow-dipping normal faults in the Woodlark-D'Entrecasteaux extensional province, Papua New Guinea, *Geology*, **19**, 1205-1208.

Abers, G. A., C. Z. Mutter & J. Fang, 1997, Shallow dips of normal faults during rapid extension: Earthquakes in the Woodlark-D'Entrecasteaux rift system, Papua New Guinea, *J. Geophys. Res.*, **102**, 15301-15317.

Amelung, F. & G. King, 1997, Earthquake scaling laws for creeping and non-creeping faults, *Geophys. Res. Lett.*, **5**, 507-510.

Anderson, E. M., 1951, *The dynamics of faulting and dyke formation*, Oliver and Boyd, Edinburgh, 206 p,

Armijo, R., P. Tapponnier, J. L. Mercier & H. Tong-Lin, 1986, Quaternary extension in southern Tibet: Field observations and tectonic implications, *J. Geophys. Res.*, **91**, 13803-13872.

Bernard, P., et al., 1997, The M_s=6.2, June 15, 1995 Aigion earthquake (Greece): Evidence for low angle normal faulting in the Corinth rift, *J. of Seis.*, **1**, 131-150.

Byerlee, J., 1978, Friction of rocks, *Pure and Appl. Geophys.,* **116**, 615-626.

Braunmiller, J. & J. Nabelek, 1996, Geometry of continental normal faults: Seismological constraints, *J. Geophys. Res.*, **101**, 3045-3052.

Buck, W. R., 1988, Flexural rotation of normal faults, *Tectonics*, **7**, 959-973.

Carpenter, B. M., C. Marone & D. M. Saffer, 2011, Weakness of the San Andreas Fault revealed by samples from active fault zones, *Nature Geoscience*, **4**, 251-254.

Carpenter, S., J. Nabelek & J. Braunmiller, 2010, South-central Tibetan seismicity from HiCLIMB seismic array data, *EOS Trans. AGU*, **91**, Fall Meeting Suppl., Abstract T43B-2223.

Cogan, M. J., K. D. Nelson, W. S. F. Kidd, C. Wu & Project INDEPTH Team, 1998, Shallow structure of the Yadong-Gulu ridf, southern Tibet, from refraction analusis of Project INDEPTH common midpoint data, *Tectonics*, **17**, 46-61.

Copley, A., J.-P. Avouac & B. P. Wernicke, 2011, Evidence for mechanical coupling and strong Indian lower crust beneath southern Tibet, *Nature*, **472**, doi:10.1038/nature09926.

Collettini, C. & R. H. Sibson, 2001, Normal faults, normal friction?, *Geology*, **29**, 927-930.

Doser, D. I., 1987, The Ancash, Peru, earthquake of 1946 November 10: Evidence for low-angle normal faulting in the high Andes of northern Peru, *Geophys. J. Royal Astron. Soc.*, **91**, 57-71.

Elliott, J. R., R. J. Walters, P. C. England, J. A. Jackson, Z. Li & B. Parsons, 2010, Extension on the Tibetan plateau: Recent normal faulting measured by InSAR and body wave seismology, *Geophys. J. Int.*, **183**, 503-535.

Eyidogan, H. & J. Jackson, 1985, A seismological study of normal faulting in the Demirci, Alasehir and Gediz earthquakes of 1969-70 in western Turkey: Implications for the nature and geometry of deformation in the continental crust, *Geophys. J. Royal Astron. Soc.*, **81**, 569-607.

Hatzfeld, D., et al., 1996, The Galaxidi earthquake of 18 November 1992: A possible asperity within the normal fault system of the Gulf of Corinth (Greece), *Bull. Seis. Soc. Am.*, **86**, 1987-1991.

Jackson, J. A. & N. J. White, 1989, Normal faulting in the upper continental crust: Observations from regions of active extension, *J. Struc. Geol.*, **11**, 15-36.

Kapp, P., M. Taylor, D. Stockli & L. Ding, 2008, Development of active low-angle normal fault systems during orogenic collapse: Insight from Tibet, *Geology*, **36**, 7-10.

Langin, W. R., L. D. Brown & E. Sandvol, 2003, Seismicity of central Tibet from Project INDEPTH III seismic recordings, *Bull. Seis. Soc. Am.*, **93**, 2146-2159.

Lister, G. S. & G. A. Davis, 1989, The origin of metamorphic core complexes and detachment faults formed during the Tertiary continental extension in the northern Colorado River region, USA, *J. Struc. Geol.*, **11**, 65-93.

McCaffrey, R. & J. Nabelek, 1998, Role of oblique convergence in the active deformation of the Himalayas and southern Tibet plateau, *Geology*, **26**, 691–694.

Melosh, H. J., 1990, Mechanical basis for low-angle normal faulting in the Basin and Range province, *Nature*, **43**, 331-335.

Moore D. E. & D. A. Lockner, 2008, Talc friction in the temperature range 25°-400°C: Relavance for fault-zone weakening, *Tectonophyics*, **449**, 120-132.

Nabelek, J. & G. Xia, 1995, Moment-tensor analysis using regional data: Application to the 25 March, 1993, Scotts Mills, Oregon, earthquake, *Geophys. Res. Lett.*, **22**, 13-16.

Nabelek, J., G. Hetenyi, J. Vergne, S. Sapkota, B. Kafle, M. Jiang, H. Su, J. Chen, B. S. Huang & the H. C. Team, 2009, Underplating in the Himalaya-Tibet collision zone revealed by the Hi-CLIMB experiment, *Science*, **325**, 1371-1374.

Pavlis, G. L., F. Vernon, D. Harvey & D. Quinlan, 2004, The generalized earthquake-location (GENLOC) package: An earthquake-location library, *Computers & Geosciences*, **30**, 1079-1091.

Sibson, R. H., 1985, A note on fault reactivation, *J. Struc. Geol.*, **7**, 751-754.

Spencer, J. E. & C. G. Chase, 1989, Role of crustal flexure in initiation of low-angle normal faults and implications for structural evolution of the Basin and Range province, *J. Geophys. Res.*, **94**, 1765-1775.

Waldhauser, F. & W. L. Ellsworth, 2000, A double-difference earthquake location algorithm: Method and application to the Northern Hayward Fault, California, *Bull. Seis. Soc.Am.*, **90**, 1353-1368.

Wernicke, B., 1995, Low-angle normal faults and seismicity: A review, *J. Geophys. Res.*, **100**, 20159-20174.

Westaway, R., 1999, The mechanical feasibility of low-angle normal faulting, *Tectonophysics*, **308**, 407-443.

A2.8 Figure Captions

Figure S2-1. Map of the Pumqu-Xianza Rift. PXR fault scarps were identified from satellite imagery; tick marks indicate clear hanging-wall slip directions. Gyaring Co Transform fault (GCT) and Yarlung-Tsangpo Suture (YTS) are also plotted. Nearby HiCLIMB seismic stations indicated by yellow triangles. International Seismological Center (ISC) earthquake locations are shown as open circles (red: 1980s, black: 1994-2012). Blue dots are epicenters from the Carpenter et al. (2010) HiCLIMB catalog

within the black-dashed box. Black diamonds are towns. White box is area of Fig. S2-2. Upper inset shows histogram of ISC reported ($m_b \geq 4.0$) seismicity. Lower inset shows HiCLIMB phase-2 stations; YTS and BNS (Bangong-Nujiang Suture) bound the Lhasa Block. Black box shows the area of the main figure.

Figure S2-2. Epicenters for manually located earthquakes, blue for events west of the Qingdu segment and red for events near T0370. White dots are epicenters from the Carpenter et al. (2010) HiCLIMB catalog. White line shows profile location for Fig. S2-3. Fault plane solutions from RMT analysis are identified by event date (YYMMDD) and color-coded by faulting type. Complete results are provided in the electronic supplement. Teleseismic ISC locations for 6 earthquakes (black circles) relocate into the blue cluster. Delineated faults are as in Fig. S2-1.

Figure S2-3. Shaded relief map highlighting topography (top) and possible tectonic interpretations (bottom). Highest quality hypocenters (best geometrical coverage) follow Fig. S2-2 color scheme. Receiver function velocity model from Nabelek et al. (2009) is embedded to the left within profile view. Horizontal black dashed line marks the top of the low-velocity zone, likely corresponding to base of the seismogenic upper crust. Possible faulting interpretations illustrated: planar 29° west-dipping low-angle fault surfacing at the PXR east wall (red dashed line), west-dipping listric fault (black dash-dotted line), and planar high-angle 61° east-dipping fault (black dotted

line). Only the 29° west-dipping fault interpretation is associated with a surface expression.

Figure S2-4. Ratio of effective principal stresses (R) for reactivation of a cohesionless fault plotted against normal fault dip (after Collettini & Sibson, 2001) for vertical principal stress (σ_1). For normal friction, m=0.6, a fault dipping ≤30° is completely locked and cannot move; slip on faults dipping between 30° and 40° requires high stress ratios making slip less likely as dip decreases. A reduction to μ = 0.3-0.4 is necessary to accommodate slip along faults with 22°-33° dip. Dashed line indicates approximate dip limit for active slip, about 40° under normal conditions (μ=0.6), as indicated by global observations.

Figure S2-5. Velocity models used for hypocenter and RMT determination: receiver function model from Nabelek et al. (2009) (black), 8-layer model retaining receiver function overall layer slowness (red), and model based on P_g and P_n travel times (green). Note: this is Figure S1 in GJI publication.

Figure S2-6. Example of RMT inversion for event 040723_0125. Observed (black) and synthetic (red) seismograms for a few select stations in each 30° azimuthal sector used for inversion. Right shows variance of fit as a function of depth (bottom) and changes in strike, dip, and rake relative to the best double couple solution (179°/29°/–82°) (top). Confidence intervals mentioned in the text and listed in Table S2-2 are

based on a conservative 5% variance increase. Triangles along the circumference of the focal mechanism on bottom show azimuthal station distribution, red triangles are stations shown above. Note: this is Figure S2 in GJI publication.

A2.9 Table Captions

Table S2-1. Hypocenter locations of 50 earthquakes in the PXR region determined in this study using the receiver function velocity model (Fig. S2-5). Columns are: Event date, time, latitude, longitude, depth, number of P-and S-arrivals used, horizontal 1-σ error ellipse (columns 7 to 9), and local magnitude. We utilized 105 broadband and 3 short-period stations with sample rates of 50 or 100 Hz. For the three earliest events, not all close-by stations were operating resulting in larger uncertainties. Their apparent slight west-shift (see also Fig. S2-2) is an artifact; hypoDD relative location (Waldhauser & Ellsworth, 2000) moved these events east into the remaining cluster. Station outages beginning in November 2004 reduced near-by coverage for 7 western cluster events. We do not show these 10 events in Fig. S2-3. Note: this is Table S1 in GJI publication.

Table S2-2. Source parameters of 12 earthquakes from regional moment tensor (RMT) analysis in the 20-50 s period band. Columns left to right are: Event date and origin time; strike, dip and rake for nodal plane 1; uncertainties for nodal plane 1; strike, dip and rake for nodal plane 2; RMT depth; RMT depth uncertainty; moment

magnitude; number of seismic stations used in RMT analysis; and percent double couple for each solution. Asterisk denotes the event analyzed in the 10-30 s band. Uncertainties are based on 5% variance increase. Note: this is Table S2 in GJI publication.

Figure S2-1

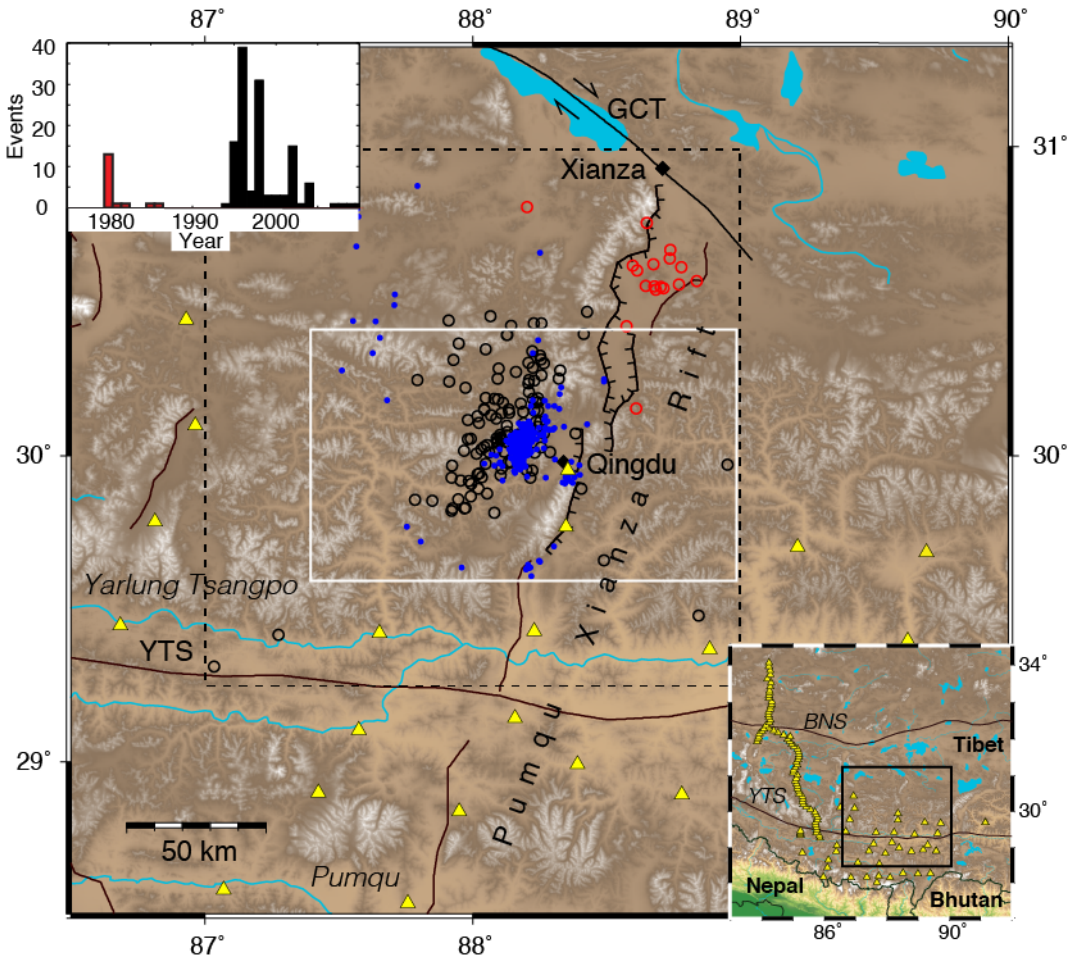
87°
88°
89°
90°
31°
30°
29°
34°
Events
40
30
20
10
0
1980
1990
2000
Year
GCT
Xianza
Qingdu
Yangbajain Rift
Xianza Rift
Pumqu Rift
Yarlung Tsangpo
YTS
50 km
Pumqu
BNS
Tibet
Nepal
Bhutan
86°
90°

Figure S2-2

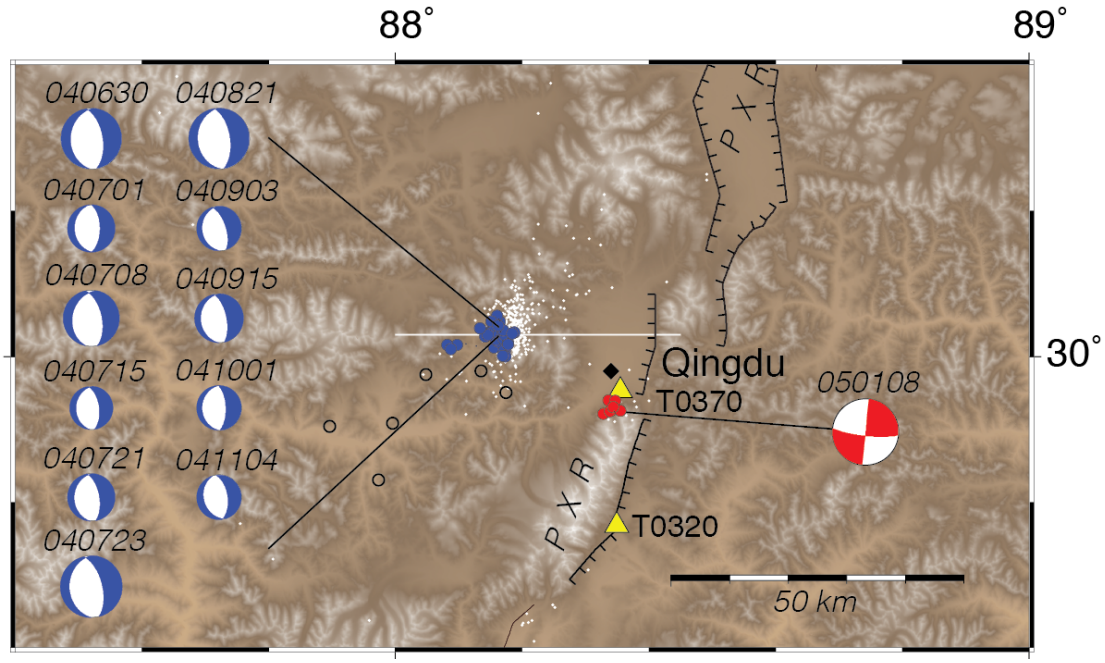
88°
89°
30°
040630
040821
040701
040903
040708
040915
040715
041001
040721
041104
040723
P X R
Qingdu
T0370
050108
T0320
50 km

Figure S2-3

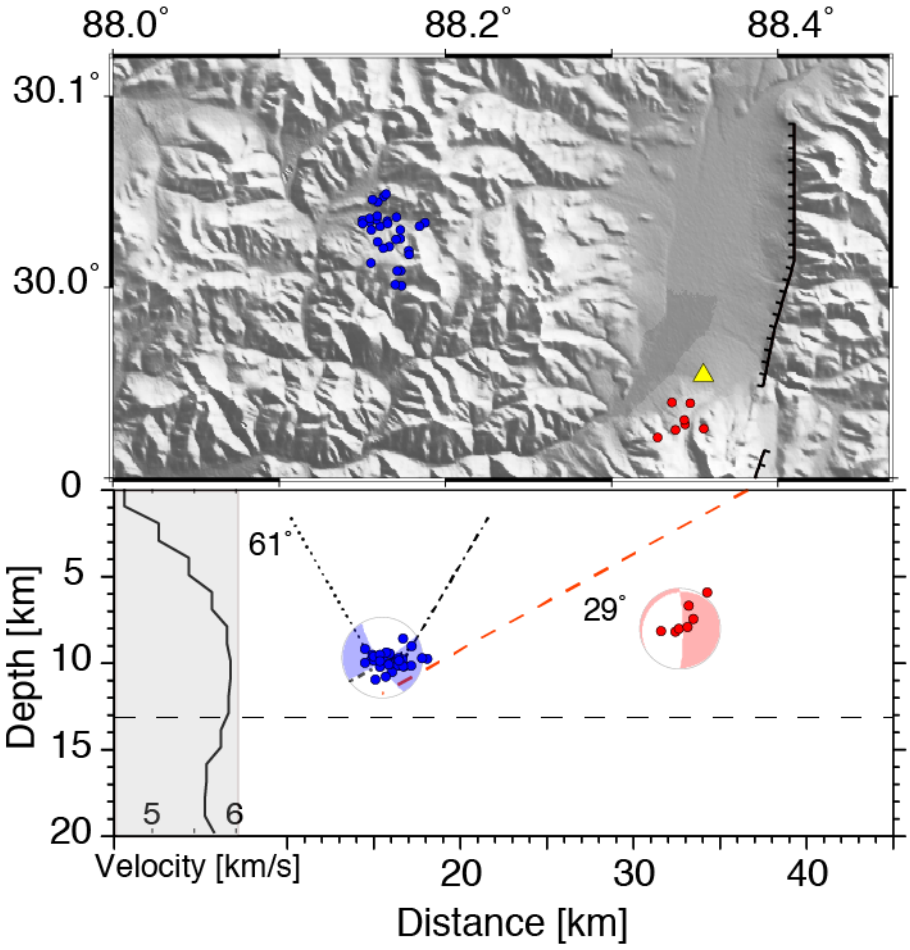
88.0°
88.2°
88.4°
30.1°
30.0°
0
5
10
15
20
Depth [km]
61°
29°
5
6
Velocity [km/s]
20
30
40
Distance [km]

Figure S2-4

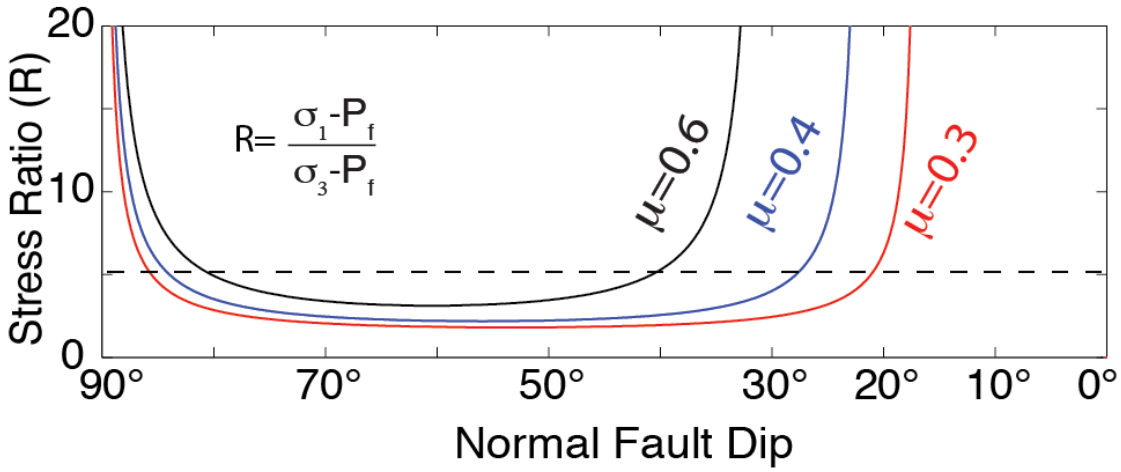
20
10
0
Stress Ratio (R)
R= σ1-Pf / σ3-Pf
μ=0.6
μ=0.4
μ=0.3
90°
70°
50°
30°
20°
10°
0°
Normal Fault Dip

Figure S2-5

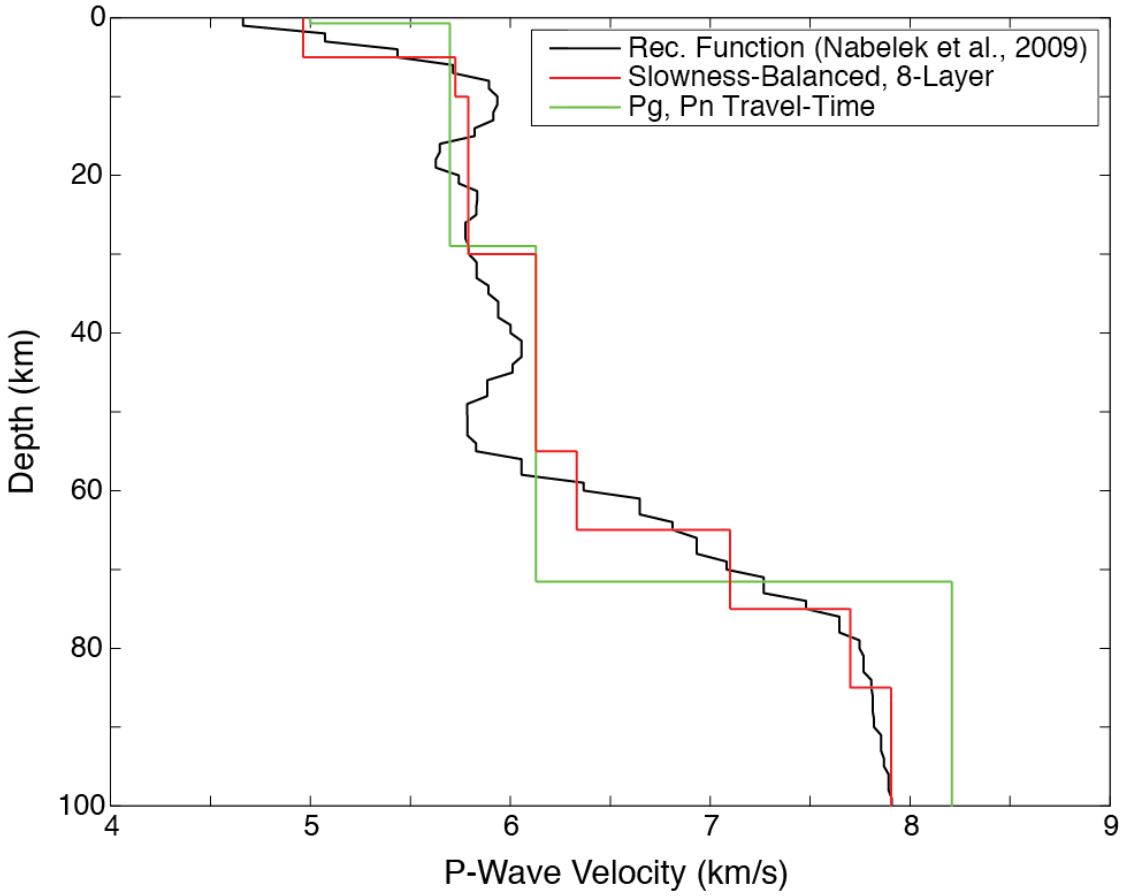
Rec. Function (Nabelek et al., 2009)
Slowness-Balanced, 8-Layer
Pg, Pn Travel-Time
Depth (km)
0
20
40
60
80
100
4
5
6
7
8
9
P-Wave Velocity (km/s)

Figure S2-6

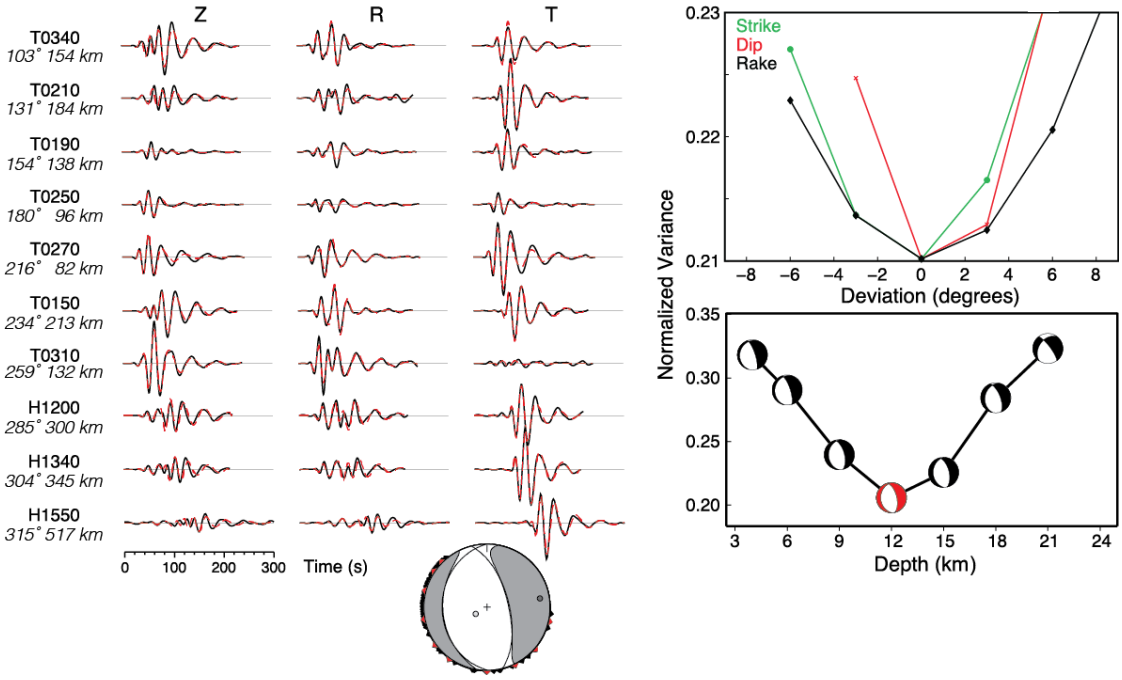
Z
R
T
T0340
103° 154 km
T0210
131° 184 km
T0190
154° 138 km
T0250
180° 96 km
T0270
216° 82 km
T0150
234° 213 km
T0310
259° 132 km
H1200
285° 300 km
H1340
304° 345 km
H1550
315° 517 km
0
100
200
300
Time (s)
Strike
Dip
Rake
Normalized Variance
Deviation (degrees)
Depth (km)

Table S2-1

Event Date YYMMDD	Event Time HH:MM:SS.SS	Lat (°N)	Lon (°E)	Depth (km)	Arrivals #	Ellipse Strike (°)	Ellipse Axis Major (km)	Ellipse Axis Minor (km)	M_L
040630	15:33:01.00	30.017	88.097	11.9	94	293	2.4	2.3	4.9
040701	19:14:35.69	30.016	88.082	12.0	94	242	3.0	1.4	4.0
040703	02:11:23.12	30.011	88.088	11.4	71	239	2.3	1.5	3.5
040708	11:29:35.34	30.034	88.154	9.7	119	24	1.2	0.7	3.8
040708	21:49:55.67	30.032	88.161	9.7	124	22	1.2	0.6	4.6
040709	06:34:24.37	30.021	88.166	10.5	98	20	1.3	0.6	3.8
040711	00:38:46.76	30.036	88.159	9.6	79	25	1.4	0.7	3.3
040715	23:39:27.48	30.026	88.173	9.8	108	20	1.4	0.6	3.7
040719	10:03:34.06	30.035	88.165	9.4	83	27	1.5	0.7	3.7
040721	15:44:00.13	30.035	88.150	9.2	111	23	1.3	0.6	4.0
040721	17:54:31.44	30.036	88.155	9.5	79	26	1.5	0.6	3.1
040723	01:25:29.34	30.013	88.155	9.8	116	24	1.2	0.5	5.0
040724	02:51:08.38	30.021	88.163	10.8	91	23	1.4	0.6	3.4
040728	02:18:33.93	30.030	88.155	9.6	89	21	1.3	0.6	3.7
040728	04:19:24.79	30.009	88.173	8.6	73	27	1.6	0.8	3.3
040803	07:04:16.70	30.009	88.171	10.1	84	22	1.4	0.7	3.4
040805	20:35:27.07	30.034	88.165	10.0	87	20	1.4	0.6	3.4
040809	22:07:02.33	30.048	88.163	9.4	92	25	1.6	0.7	3.4
040811	13:17:45.94	30.001	88.174	10.2	86	22	1.7	0.7	3.7
040811	14:24:10.03	30.001	88.170	10.1	84	22	1.6	0.7	3.6
040818	20:01:33.87	30.024	88.159	9.5	81	22	1.6	0.7	3.4
040820	10:46:08.17	30.025	88.170	9.7	80	24	1.6	0.7	3.7
040821	02:06:07.40	30.049	88.164	10.1	74	23	1.9	0.7	3.7
040821	09:07:06.63	30.037	88.159	10.2	103	26	1.4	0.6	5.0
040821	19:06:20.68	30.019	88.178	10.1	86	24	1.5	0.6	3.4
040824	18:15:36.85	30.030	88.173	10.2	60	22	1.7	0.7	3.2
040824	21:23:41.12	30.037	88.170	9.8	57	23	1.7	0.7	3.4
040827	05:46:20.79	30.034	88.188	9.7	49	23	1.9	0.8	3.0
040831	01:12:56.25	30.017	88.178	9.0	76	24	1.6	0.7	3.6
040831	09:27:20.72	30.032	88.184	9.7	48	20	1.9	0.8	3.4
040903	10:24:41.29	30.033	88.150	10.0	88	22	1.6	0.7	3.8
040915	13:10:52.68	30.045	88.159	9.9	99	20	1.6	0.7	4.1
041001	18:03:24.95	30.046	88.156	10.9	96	19	1.7	0.7	3.8
041104	14:00:58.24	30.056	88.161	9.6	66	28	2.1	0.8	3.8
041109	12:15:57.52	30.049	88.152	9.5	64	22	1.7	0.8	3.5
041111	17:50:12.73	30.028	88.142	10.6	60	24	1.9	0.8	3.7
041111	22:23:09.31	30.034	88.152	10.1	29	22	2.3	0.9	3.4
041112	11:05:18.67	30.030	88.146	9.7	62	27	1.9	0.8	3.6
041229	03:24:11.31	29.928	88.344	6.7	37	33	1.7	0.9	2.1
041229	21:05:26.27	29.926	88.355	5.9	14	39	1.9	1.1	2.1
050101	22:46:21.49	29.921	88.328	8.1	66	24	1.5	0.8	3.6
050104	00:30:48.02	29.940	88.336	8.2	39	29	2.0	0.9	2.4
050107	21:10:46.49	29.939	88.347	7.4	25	34	1.9	1.0	2.3
050108	12:51:08.75	29.925	88.338	8.0	60	34	1.7	0.8	3.3
050116	04:55:18.89	29.931	88.344	7.9	33	31	1.9	1.0	2.2
050121	14:57:25.85	30.043	88.162	10.0	71	25	2.3	0.8	3.8
050222	03:47:32.01	30.039	88.133	6.1	51	33	3.0	0.9	3.3
050222	23:38:25.54	29.643	88.209	5.8	30	31	1.4	1.0	2.5
050223	03:30:07.95	29.645	88.214	5.2	33	40	1.5	1.2	2.5
050604	20:44:14.54	29.707	88.304	6.0	28	38	1.3	1.0	2.2

Table S2-2

Event Time/ID (YYMMDD_HHMM)	S1/D1/R1 (°/°/°)	Uncertainty (±°/±°/±°)	S2/D2/R2 (°/°/°)	RMT Depth (km)	Uncertainty (km)	M_w	Stations (#)	DC (%)
040630_1533	183/32/-79	6/4/10	350/59/-97	12	-2/+2	4.2	54	83
040701_1914	177/30/-92	10/7/13	360/60/-89	12	-5/+2	3.5	24	95
040708_2149	191/33/-70	10/9/14	348/59/-102	12	-5/+5	4.1	21	99
040715_2339	183/30/-81	13/8/15	352/60/-95	12	-12/+5	3.4	45	90
040721_1544	183/29/-79	11/8/14	350/61/-96	12	-5/+5	3.7	58	83
040723_0125	179/30/-78	4/3/5	346/61/-97	12	-1/+2	4.5	83	84
040821_0907	177/30/-85	6/4/8	351/60/-93	12	-1/+2	4.5	81	94
040903_1024	176/25/-77	25/15/33	342/65/-96	12	-12/+15	3.5	23	51
040915_1310	180/26/-78	7/5/7	348/65/-96	12	-1/+3	3.8	56	77
041001_1803	175/22/-94	11/6/13	359/68/-88	15	-5/+8	3.4	32	57
041104_1400	164/32/-97	11/8/14	352/58/-86	12	-4/+5	3.7	45	79
050108_1251*	96/79/-179	18/26/24	6/89/-11	15	-9/+12	3.2	11	87